ACS NANO

www.acsnano.org

ARTICLE

Dual-Targeting Mn@CeO_2 Nanozyme-Modified Probiotic Hydrogel Microspheres Reshape Gut Homeostasis in Inflammatory Bowel Disease

Pinwen Zhou,[#] Qi Sun,[#] Longchang Huang,[#] Yufei Xia, Jiaqi Wang, Dongze Mo, Christopher J. Butch, Chenmei Li, Li Zhang, Xuejin Gao, Hui Wei,* and Xinying Wang*

Cite This: *ACS Nano* 2025, 19, 31619−31642

Read Online

ACCESS | Metrics & More | Article Recommendations | Supporting Information

ABSTRACT: Oral microecological agents show potential in reshaping intestinal microbiota and treating inflammatory bowel disease (IBD), but their clinical application is hindered by gastrointestinal challenges, antioxidant instability, and ineffective targeted delivery. In this study, we proposed a protective modification strategy utilizing a nanozyme coating and an alginate microsphere system to enhance the delivery efficiency, effectiveness, and precision of probiotics. By incorporating Mn into CeO_2, Mn@CeO_2 nanozyme was synthesized, significantly boosting ROS scavenging activity both *in vitro* and *in vivo* at safe dosages. Following the coincubation of Mn@CeO_2 with *Limosilactobacillus reuteri*, the nanozymes were successfully distributed onto the surface of the probiotics. MnCe@LR/AMs were then fabricated using the electrostatic spray method, enhancing their tolerance to the acidic environment of the stomach. Notably, sodium alginate (SA), through electrostatic interactions and binding to mannose receptors highly expressed at inflamed sites, conferred a dual-targeting property to MnCe@LR/AMs. In the treatment of colitis in mice, MnCe@LR/AMs were shown to function through the synergistic antioxidant and anti-inflammatory activities of their components. They also effectively reinforced the intestinal barrier, while improving gut microbial diversity and increasing the relative abundance of probiotics. Furthermore, we demonstrated that MnCe@LR/AMs contribute to the maintenance of intestinal homeostasis by enhancing the absorption of amino acids in the gut and modulating macrophage polarization to regulate the immune response. These findings suggest that MnCe@LR/AMs hold significant promise for developing advanced IBD therapies, offering improved precision and efficacy in probiotic delivery.

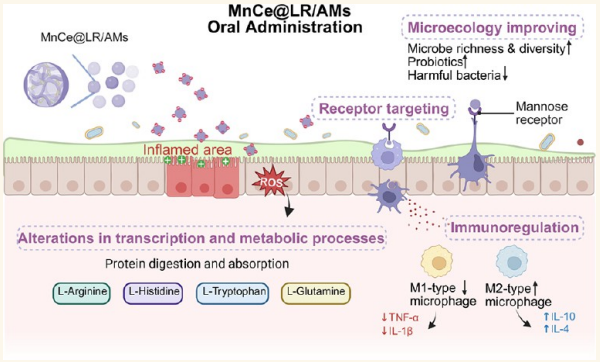

KEYWORDS: *inflammatory bowel disease, probiotic delivery, nanozyme, microspheres, gut microbiota, oxidative stress*

Inflammatory bowel disease (IBD) is a chronic inflammatory disorder of the gastrointestinal tract, where the intricate interplay between gut dysbiosis, intestinal barrier dysfunction, and immune dysregulation drives disease progression.[1,2] Mounting evidence indicates that microbial imbalance in IBD patients results in excessive reactive oxygen species (ROS) production, leading to epithelial cell damage, compromised barrier integrity, and increased intestinal permeability.[2,3] The combined effects of oxidative stress and barrier impairment stimulate abnormal immune cell activation, particularly macrophages, resulting in excessive release of pro-inflammatory cytokines. This immune dysregulation further aggravates barrier damage and oxidative stress, creating a self-perpetuating cycle of chronic inflammation.[4]

The growing global prevalence of IBD presents substantial healthcare and economic challenges.[5] Current treatment strategies, while providing symptomatic relief, often fail to effectively interrupt this inflammatory cycle and may lead to

Received: May 29, 2025
Revised: July 31, 2025
Accepted: August 1, 2025
Published: August 25, 2025

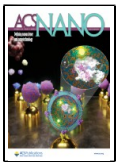

Scheme 1. Schematic Outlines the Preparation of Dual-Inflammatory-Targeting Probiotic-Nanozyme Hydrogel Microspheres for Colitis Treatment[a]

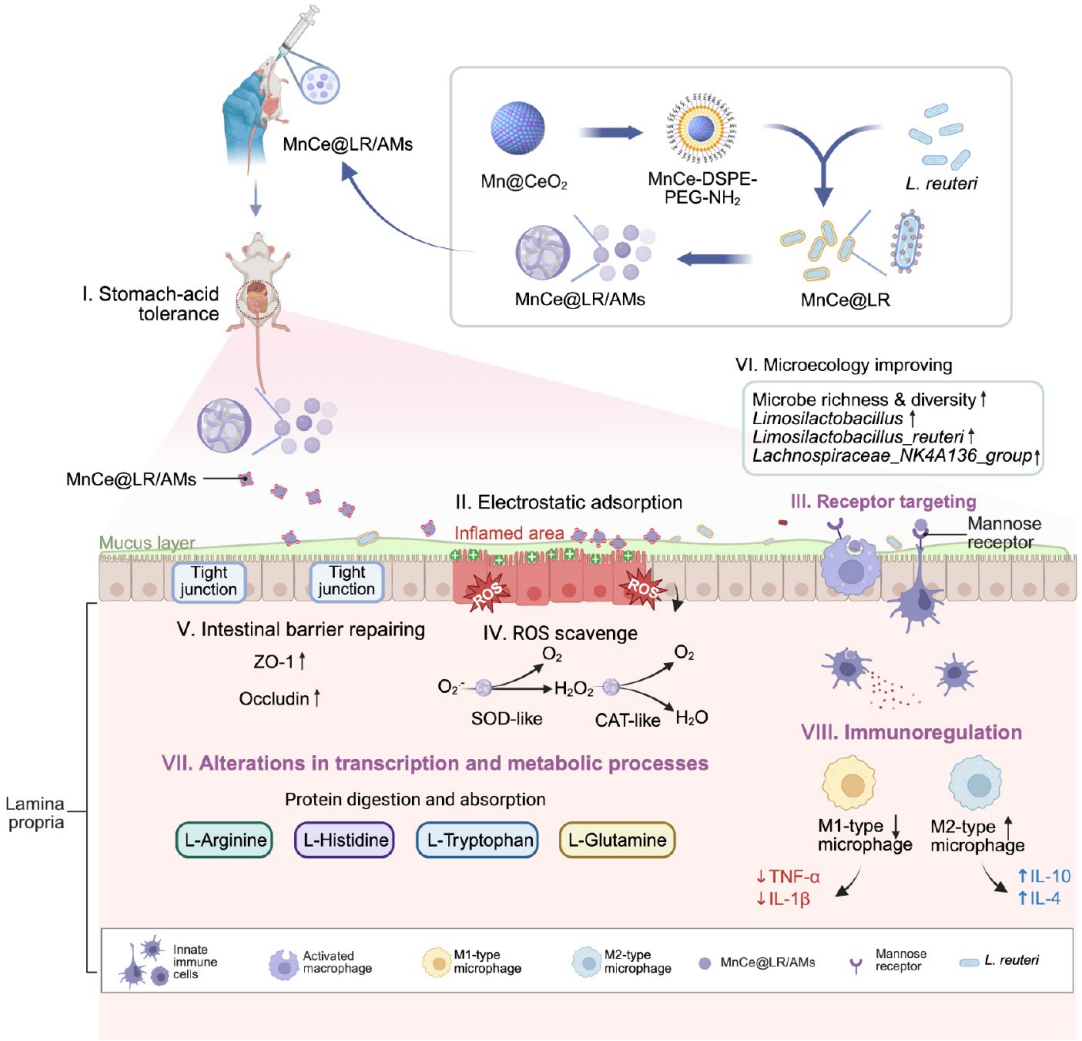

[a]MnCe@LR/AMs, synthesized from $Mn@CeO_2$ nanozymes, demonstrate: (I) Stomach acid tolerance; (II–III) Adhesion to inflammation sites via electrostatic and MR targeting; (IV) ROS scavenge; (V) Intestinal barrier repairing; (VI) Microecology improving; (VII) Alterations in transcription and metabolic processes; (VIII) Immunoregulating. Created in BioRender. Zhou, P. (2025) https://BioRender.com/znl2iv2.

serious complications with prolonged use, including increased susceptibility to infections and malignancy.[6] Probiotic-based therapies have emerged as a promising alternative approach by restoring microbial balance and enhancing barrier function.[7] However, their therapeutic potential is limited by poor bacterial survival in the hostile inflammatory microenvironment of IBD and insufficient capacity to eliminate excessive ROS.[8] These limitations contribute to suboptimal treatment outcomes and extended therapy durations. Consequently, there is an urgent need for innovative probiotic delivery systems that can simultaneously achieve targeted release at inflamed sites, improve bacterial viability, and enhance ROS scavenging capacity, thereby effectively disrupting the inflammatory cascade and promoting restoration of intestinal homeostasis.

With the rapid advancement of nanotechnology, engineered nanomaterials exhibiting enzyme-mimicking activities have been developed to address the inherent instability of natural enzymes, collectively termed "nanozymes".[9] Both natural antioxidant molecules[10] and nanozymes[11] have recently garnered significant attention in ROS-scavenging research. While both show promise in reducing ROS levels, they exhibit inherent limitations: antioxidant molecules possess excellent biocompatibility and intestinal absorption but suffer from low reaction rates, nonspecific scavenging, and insufficient treatment efficiency; nanozymes offer catalytic stability, superior environmental tolerance, lower cost, easier preparation, and facile surface modification, yet face challenges in biosafety and potential toxicity.[12] Over the past few years, cerium oxide nanozyme (CeO_2)[13] has attracted significant attention for biomedical applications because of their excellent ROS-scavenging properties and biocompatibility. However, enhancing the catalytic activity of nanozyme while ensuring biosafety remains a critical challenge for clinical translation. A recent study demonstrated that manganese/cerium mixed-metal nanozymes are more effective in treating acute radiation-induced damage in mice than their individual manganese or cerium counterparts,[14] suggesting that mixed-metal nanozymes can maintain efficacy at lower doses while ensuring biosafety. Furthermore, manganese doping into CeO_2 significantly enhances oxygen vacancy formation, which modulates oxygen diffusion and storage

https://doi.org/10.1021/acsnano.5c08999
ACS Nano 2025, 19, 31619–31642

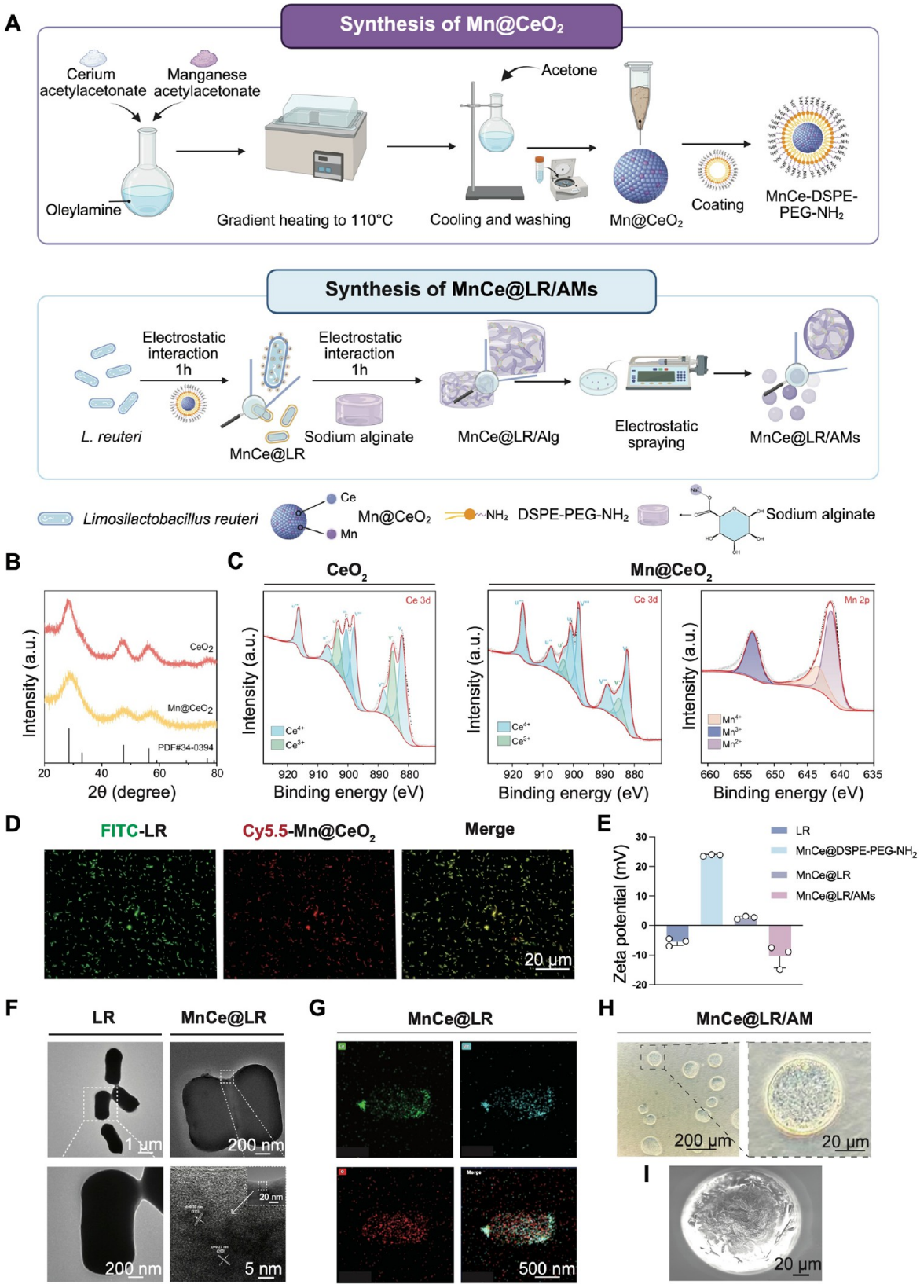

Figure 1. Construction and Characterization of MnCe@LR/AMs. (A) Preparation procedure for $Mn@CeO_2$ and MnCe@LR/AMs. Created in BioRender. Zhou, P. (2025) https://BioRender.com/uw4a1j6. (B) XRD pattern of $Mn@CeO_2$. (C) XPS analysis of CeO_2 and $Mn@CeO_2$. (D) Typical confocal images of MnCe@LR, with the green channel showing FITC-labeled *L. reuteri* and the red channel showing Cy5.5-labeled MnCe@DSPE-PEG-NH_2. Scale bar: 20 μm. (E) Zeta potential distribution of *L. reuteri*, MnCe@DSPE-PEG-NH_2, MnCe@LR, and MnCe@LR/AMs. (F) TEM images of LR and MnCe@LR. Scale bars: 1 μm, 200 and 5 nm. (G) EDS images of MnCe@LR. Scale bar: 500 nm. (H) Light microscope image of MnCe@LR/AMs. Scale bars: 200 and 20 μm. (I) SEM image of MnCe@LR/AMs. Scale bar: 20 μm. Data are presented as the means ± SD (n = 3).

https://doi.org/10.1021/acsnano.5c08999
ACS Nano 2025, 19, 31619−31642

capacity through manganese's mixed-valence states, thereby markedly improving the nanozyme's ROS scavenging efficacy.[15] Thus, we hypothesized that manganese/cerium mixed-metal nanozymes could offer substantial therapeutic potential in treating IBD.

Limosilactobacillus reuteri (*L. reuteri*), a well-recognized probiotic, has shown potential in alleviating intestinal inflammation and improving IBD by enhancing gut metabolism and restoring the microbiota balance.[2,16] However, conventional delivery strategy face limitations, such as low intestinal colonization rates, poor targeting, and their inability to simultaneously scavenge ROS to establish a favorable growth microenvironment.[17] Previous studies have demonstrated that engineered *Bifidobacterium longum* modified with artificial enzymes exhibits superior therapeutic efficacy in IBD treatment through sustained ROS scavenging.[18] However, this system relies on bacterial adhesion proteins for colon targeting, limiting its universality as a broad-spectrum strain delivery platform. Additionally, the absence of a protective system leads to limited enhancement of bacterial viability provided by the SAzyme coating when exposed to simulated gastric and intestinal fluids (SGF/SIF). Prior studies have suggested that sodium alginate (SA) is an effective carrier for protecting, delivering, and sustaining the release of bioactive substances.[19] SA, a natural polysaccharide obtained from brown algae, is made up of β-D-mannuronic acid (M) and α-L-guluronic acid (G) units linked by (1→4) bonds. The M group of SA attaches to mannose receptors (MR) on the surfaces of antigen-presenting cells, providing potential targeting to MR-overexpressing inflamed regions.[20] In addition, as an FDA-approved food additive, the acid resistance of SA makes it an ideal material for bacterial encapsulation, effectively shielding probiotics from low gastric pH and providing physical protection during intestinal transit. This suggests that alginate-based microspheres could significantly enhance the colonization rate and delivery efficiency of *L. reuteri*. Past research has primarily focused on the physical protective capacity and unique pH-responsive properties of sodium alginate.[21] However, its potential dual-targeting characteristics for IBD therapy remain unexplored.

In this study, we developed a probiotic delivery system using inflammation-specific targeting MnCe@LR/AMs (Scheme 1). By introducing Mn into CeO_2, we synthesized Mn@CeO_2 nanozyme, which not only ensured biological safety, but also enhanced the superoxide dismutase (SOD)-like and catalase (CAT)-like enzymatic activities of CeO_2 at the same concentration. Following successful construction of the probiotic nanozyme coating, we fabricated alginate-based microspheres that exhibited acid resistance and inflammation targeting. We found that MnCe@LR/AMs could effectively target intestinal inflammation through electrostatic attraction and by binding to MRs that are highly expressed at inflamed sites, thereby enhancing the delivery efficiency and precision of probiotics. Moreover, MnCe@LR/AMs exerted anti-inflammatory effects by reducing intestinal ROS and protecting the intestinal barrier while also promoting gut microbiota diversity and richness, thus remodeling the intestinal microecology. In terms of regulating gut gene transcription and metabolism, MnCe@LR/AMs enhanced the synthesis and metabolism of important amino acids, such as histidine and arginine, thereby improving protein digestion and absorption. Furthermore, MnCe@LR/AMs exhibited immunomodulatory effects by regulating macrophage differentiation. In conclusion, this study offers an innovative approach to deliver probiotics via nanozyme modification and alginate microspheres, thereby providing new therapeutic insights and alternative strategies for IBD treatment.

RESULTS

Construction and Characterization of MnCe@LR/AMs.

L. reuteri is a well-known probiotic recognized for its excellent biocompatibility, anti-inflammatory effects, microbiota-modulating properties, and is commonly employed in treating a range of gastrointestinal disorders.[22] Prior researches have shown that *L. reuteri* can exert therapeutic effects on IBD by enhancing intestinal barrier function, regulating gut microbiota balance, and immune modulation (Figure S1).[23] Therefore, we selected *L. reuteri* as a model strain, and constructed a manganese-doped CeO_2 (Mn@CeO_2) nanozyme-coating on its surface. Modified *L. reuteri* was encapsulated in alginate-based microspheres using electrostatic spraying.

We chose Mn@CeO_2 as the coating material to enhance the enzymatic catalytic activity of probiotics and further improve ROS-scavenging ability. Figures S2 and S3 present the structural characterization[24] and high-resolution transmission electron microscopy (HRTEM) images of Mn@CeO_2, respectively, and the preparation method is detailed in Figure 1A. X-ray diffraction (XRD) results (Figure 1B) confirmed the characteristic peaks of CeO_2, validating the successful synthesis of Mn@CeO_2. X-ray photoelectron spectroscopy (XPS) analysis (Figures 1C and S4) revealed the oxidation states and relative proportions of Ce, Mn, and O in CeO_2 and Mn@CeO_2. The proportion of Ce^{4+} in CeO_2 increased after the doping of Mn. Cytotoxicity of Mn@CeO_2 was assessed using the CCK-8 assay with RAW264.7 and MC-38 cell lines, and the results indicated that Mn@CeO_2 had negligible effects on cell viability with a concentration of 20 μg/mL (Figure S5). Additionally, Mn@CeO_2 (20 μg/mL) demonstrated good biocompatibility with *L. reuteri* (Figure S6).

To establish a probiotic-ROS scavenging system, Mn@CeO_2 was functionalized with DSPE-PEG-NH_2, and the functionalized MnCe@DSPE-PEG-NH_2 exhibited a positive charge (Figure 1E). We then gently mixed MnCe@DSPE-PEG-NH_2 with *L. reuteri* and incubated them to achieve electrostatic binding, FITC-labeled *L. reuteri* and Cy5.5-labeled MnCe@DSPE-PEG-NH_2 were used, and fluorescence signals were observed to confirm the formation of the nanozyme-coating on *L. reuteri* (Figure 1D). The surface charge of *L. reuteri* underwent a transition from negative to positive, with a shift from −5.59 mV to +2.65 mV (Figure 1E). As the concentration of Mn@CeO_2 increased, the zeta potential of MnCe@LR exhibited a corresponding elevation (Figure S7). Transmission electron microscopy (TEM) images (Figure 1F) revealed that MnCe@DSPE-PEG-NH_2 successfully adhered to the surface of *L. reuteri*, forming MnCe@LR. The lattice fringe spacing of 0.32 and 0.27 nm corresponded respectively to the (111) and (200) lattice planes. Further elemental mapping and energy dispersive spectroscopy (EDS) images confirmed that the nanocoating on the surface of *L. reuteri* was rich in Mn and Ce (Figure 1G). These results collectively validate the successful synthesis of MnCe@LR.

To confer inflammation-targeting properties and enhance the retention of MnCe@LR in the colon, we encapsulated MnCe@LR in an alginate hydrogel and employed electrostatic spraying to convert it into orally administrable probiotic microspheres (MnCe@LR/AMs) (Figure 1A). First, a 10 mg/mL alginate solution was heated until completely dissolved, and then cooled

https://doi.org/10.1021/acsnano.5c08999
ACS Nano 2025, 19, 31619−31642

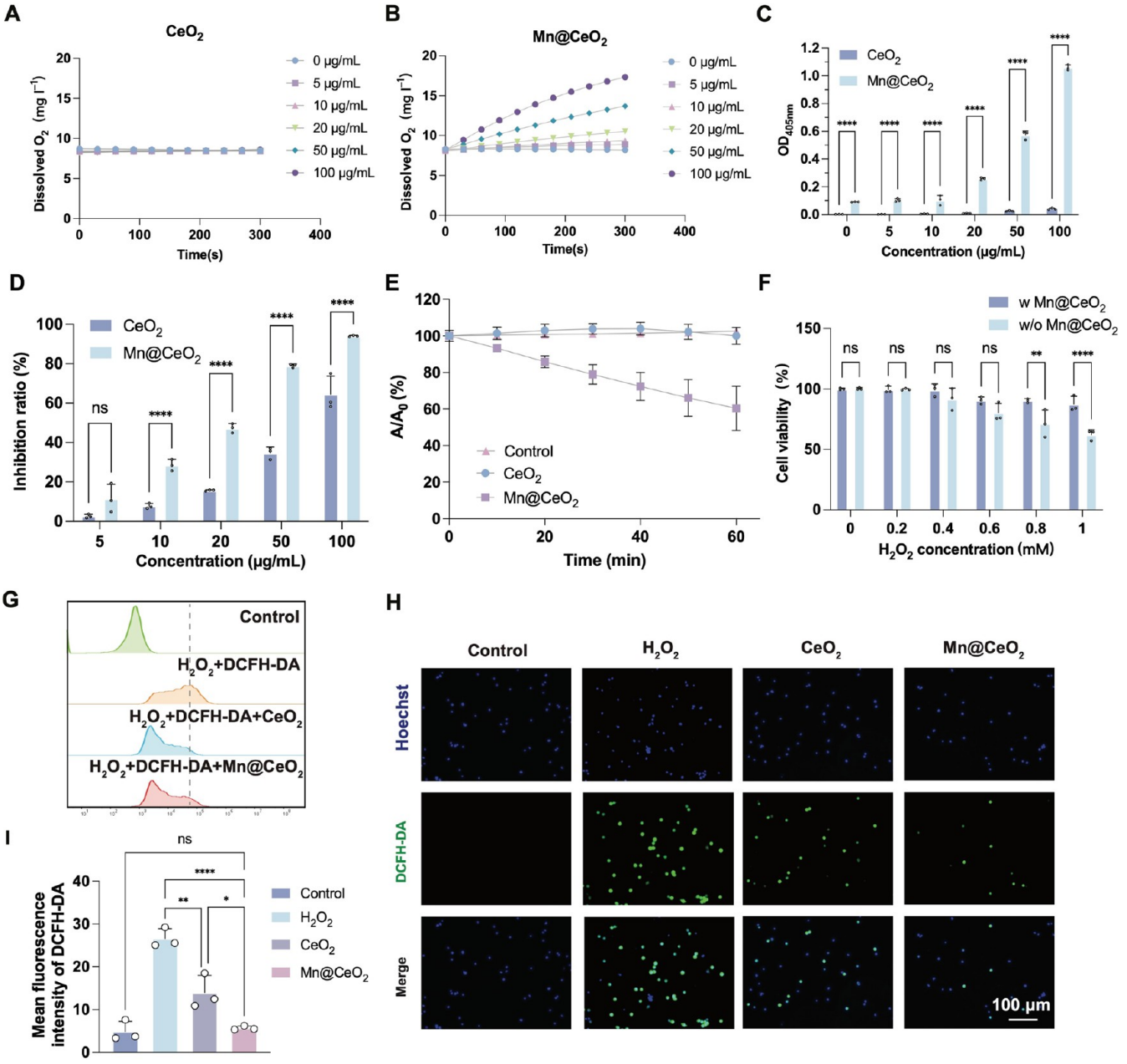

Figure 2. Antioxidant Activities of $Mn@CeO_2$ *In Vitro*. (A) Representative kinetic curves of oxygen production from the decomposition of H_2O_2 with CeO_2 at varied concentrations. (B) Representative kinetic curves of oxygen production from the decomposition of H_2O_2 with $Mn@CeO_2$ at varied concentrations. (C) CAT activities of CeO_2 and $Mn@CeO_2$ at varied concentrations. (D) SOD activities of CeO_2 and $Mn@CeO_2$ at varied concentrations. (E) *In vitro* ROS scavenging capacity of CeO_2 and $Mn@CeO_2$ measured using the ABTS probe. (F) Cell viability of RAW264.7 cells cocultured with or without $Mn@CeO_2$ under different H_2O_2 conditions, measured by CCK-8 assay. (G) ROS scavenging activities of $Mn@CeO_2$ under H_2O_2 condition with stimulated RAW264.7 cells investigated by flow cytometry. (H) ROS scavenging activities of $Mn@CeO_2$ under H_2O_2 condition with stimulated RAW264.7 cells investigated by confocal scanning laser microscopy. Scale bar: 100 μm. (I) Analysis of mean fluorescence intensity in confocal fluorescence images of $Mn@CeO_2$ under H_2O_2 condition with stimulated RAW264.7 cells. Data are presented as the means ± SD (n = 3).

naturally to 37 °C. Subsequently, MnCe@LR was added to this solution. Previous reports indicate that Ce can form complexes with alginate, further enhancing the mechanical properties of hydrogels.[25] After incubating at room temperature for 1 h, the probiotic hydrogel was electrostatically sprayed into $CaCl_2$ solution to form MnCe@LR/AMs. Scanning electron microscopy (SEM) and light microscopy revealed that the MnCe@LR/AMs exhibited uniform spherical shapes (Figure 1H,I). Particle size analysis indicated that the average diameter of MnCe@LR/AMs was 61.64 ± 20.49 μm (Figure S8). Subsequent analysis revealed that the zeta potential of MnCe@LR/AMs shifted from positive to negative, favoring the targeting of positively charged areas of colonic inflammation, thereby enabling the precise treatment of colitis (Figure 1E). The loading efficiency was quantitatively determined by inductively coupled plasma atomic emission spectroscopy (ICP-AES), revealing that after formulating $Mn@CeO_2$ into MnCe@LR/AMs, the loading efficiency of Ce and Mn elements reached 75.94% and 73.96%, respectively (Figure S9).

https://doi.org/10.1021/acsnano.5c08999
ACS Nano 2025, 19, 31619−31642

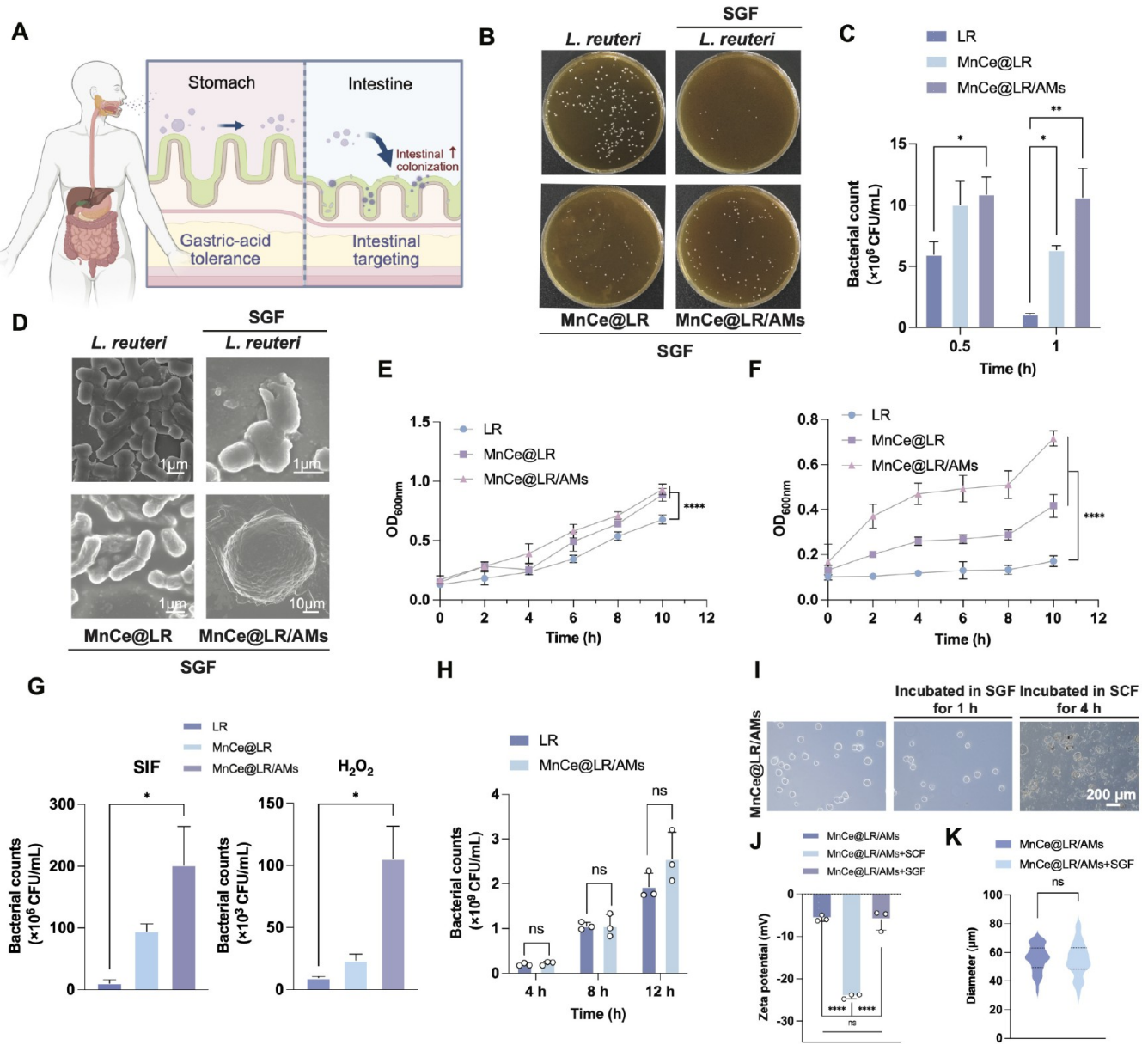

Figure 3. Resistance of modified *L. reuteri* against the gastrointestinal environment *in vitro*. (A) Schematic illustration of the nanocoating-hydrogel microsphere system enhancing intestinal colonization of probiotics. Created in BioRender. Zhou, P. (2025) https://BioRender.com/5y87pm1. (B) Representative plate count images after 1 h coincubation of *L. reuteri*, MnCe@LR, and MnCe@LR/AMs with SGF. (C) Plate count results after 0.5 and 1 h coincubation of *L. reuteri*, MnCe@LR, and MnCe@LR/AMs with SGF. (D) Representative SEM images of *L. reuteri*, MnCe@LR and MnCe@LR/AMs coincubated with SGF for 1 h. Scale bar: 1 and 10 μm. (E) Growth curves of *L. reuteri*, MnCe@LR, and MnCe@LR/AMs after 1 h coincubation with SGF, followed by transfer to MRS medium. (F) Growth curves of *L. reuteri*, MnCe@LR, and MnCe@LR/AMs in SIF without solubilization. (G) Plate count results after 2 h coincubation of *L. reuteri*, MnCe@LR, and MnCe@LR/AMs with SIF or H_2O_2. (H) Colony counting results of *L. reuteri* and MnCe@LR/AMs cultured in MRS medium at 4, 8, and 12 h time points. (I) Bright-field microscopic images of MnCe@LR/AMs after 1 h in SGF or 4 h in SCF. Scale bar: 200 μm. (J) Zeta potential measurements of MnCe@LR/AMs after 1 h in SGF or 4 h in SCF. (K) Diameter distribution of MnCe@LR/AMs before and after SGF exposure. Data are presented as the means ± SD (n = 2 for (C) and (G); n = 3 for (E), (F), (H), (J) and (K)).

Antioxidant Activities of Mn@CeO_2 and MnCe@LR/AMs *In Vitro*. Excessive ROS production leads to pathological phenomena such as lipid peroxidation and DNA damage, directly influencing the onset and progression of IBD.[26] Earlier research has demonstrated that nanozymes can significantly reduce local inflammation by reducing ROS levels. Therefore, we evaluated the enzyme-like activities of Mn@CeO_2, MnCe@LR, and MnCe@LR/AMs. First, we measured the ability of Mn@CeO_2 and CeO_2 to catalyze the production of oxygen from H_2O_2 to assess their catalase-like (CAT-like) activities. The oxygen concentration increases significantly with the increase of Mn@CeO_2 concentration. However, this phenomenon has not been observed at CeO_2 (Figure 2A,B). Using a dopamine (DA)-based standard assay, we found that the CAT activity of Mn@CeO_2 increased gradually with increasing concentration and was superior to that of CeO_2 at the same concentration (Figure 2C). Figure 2D shows that the superoxide dismutase-like (SOD-like) activity of the Mn@CeO_2 nanozyme at various concentrations exceeded that of CeO_2 at the same concentration, and increased with concentration. The findings indicated that Mn@CeO_2

https://doi.org/10.1021/acsnano.5c08999
ACS Nano 2025, 19, 31619−31642

significantly enhanced the activities of SOD-like and CAT-like enzymes due to the increase of Ce^{4+} ratio and oxygen vacancy after Mn doping (Figures 1C and S4). Subsequently, ABTS probe (a chromogenic substrate widely used in radical scavenging assays to evaluate antioxidant activity) was employed to assess the *in vitro* ROS scavenging capability of CeO_2 and Mn@CeO_2 by detecting the generation of superoxide radicals.[27] The outcomes revealed that the ROS scavenging ability of Mn@CeO_2 at the same concentration was observed to improve over time (Figure 2E). Moreover, at concentrations above 50 μg/mL, Mn@CeO_2 demonstrated significantly ROS elimination efficacy than CeO_2 (Figure S10).

To test the protective effects of Mn@CeO_2 in an ROS-rich environment, we coincubated the cells with H_2O_2 to simulate oxidative stress and assessed cell viability using the CCK-8 assay. As the H_2O_2 concentration increased, cell viability significantly decreased. However, the addition of Mn@CeO_2 at high H_2O_2 concentrations significantly improved cell survival (Figure 2F). We used DCFH-DA as a probe to quantify intracellular ROS levels and evaluate the enzyme-like activities of Mn@CeO_2 after cellular uptake. Flow cytometry analysis revealed that the mean ROS fluorescence intensity in the H_2O_2-treated group was substantially higher, whereas the ROS levels in the Mn@CeO_2-treated group were significantly lower than those in the H_2O_2-treated group and similar to those in the CeO_2 group (Figure 2G). Confocal fluorescence microscopy showed a significant increase in ROS fluorescence intensity inside the cells 30 min after H_2O_2 stimulation. After treatment with Mn@CeO_2, the fluorescence intensity significantly decreased (Figure 2H,I), indicating that the enzyme-like activity of Mn@CeO_2 effectively reduced intracellular ROS generation. The results demonstrated the effective protection of cells from inflammation-associated oxidative damage by Mn@CeO_2.

To substantiate that Mn@CeO_2 retains comparable antioxidant capacity postincorporation into MnCe@LR/AMs with context-dependent manifestation, we systematically validated their intracellular and extracellular antioxidant activities. Our study demonstrated that simulated colonic fluid (SCF) incubation significantly enhanced the extracellular SOD-like and CAT-like enzymatic activities of MnCe@LR/AMs, showing comparable efficacy to Mn@CeO_2 (Figure S11A). Further investigation into their intracellular effects revealed that while MnCe@LR/AMs coincubation elevated both CAT and SOD activities in H_2O_2-treated RAW264.7 cells, the increase was not statistically significant, indicating their limited capacity to modulate endogenous antioxidant enzyme systems (Figure S11B). Using DCFH-DA as a fluorescent probe, we quantitatively assessed the ROS-scavenging capacity of Mn@CeO_2, MnCe@LR, and MnCe@LR/AMs in cells. Immunofluorescence imaging showed markedly elevated ROS levels in H_2O_2-treated groups, whereas MnCe@LR/AMs treatment significantly reduced intracellular ROS accumulation—a finding corroborated by flow cytometric analysis (Figure S11C–E). Collectively, these results demonstrate that although MnCe@LR/AMs do not enhance intracellular CAT/SOD activities, they effectively utilize the Mn@CeO_2-derived extracellular SOD-like and CAT-like activities to mitigate ROS generation in the colonic microenvironment.

Resistance of Modified *L. reuteri* against the Gastrointestinal Environment *In Vitro*. *L. reuteri* colonization and survival in the gastrointestinal tract require tolerance to harsh conditions.[28] One of the primary challenges faced by orally administered probiotics is their endurance in the acidic environment of the stomach (Figure 3A). We examined the survival of native *L. reuteri*, MnCe@LR, and MnCe@LR/AMs in SGF. To evaluate the protective effects of the nanozyme-coating and alginate microspheres on *L. reuteri*, we incubated these three groups with SGF-containing pepsin and assessed the colony counting at different time points (Figure 3B,C). The results showed that MnCe@LR and MnCe@LR/AMs exhibited significantly higher tolerance to SGF than untreated *L. reuteri*. After 1 h of incubation, the survival rate of MnCe@LR/AMs was 9.43 times higher than that of the native *L. reuteri*. SEM revealed that after 1 h of exposure to SGF, the morphology of *L. reuteri* protected by nanozyme-coating and microspheres remained intact, whereas uncoated *L. reuteri* exhibited morphological abnormalities (Figure 3D). Confocal fluorescence imaging confirmed that *L. reuteri* remained encapsulated within MnCe@LR/AMs following 1 h incubation in SGF (Figure S12). To validate the protective effect of the nanozyme-microsphere system on *L. reuteri* proliferation in acidic environments, we measured the growth curves of the three groups in deMan Rogosa Sharpe (MRS) medium after incubation in SGF for 1 h using OD_{600} readings. The results showed that MnCe@LR and MnCe@LR/AMs maintained a more stable colony number than uncoated *L. reuteri* (Figure 3E), indicating that the system significantly enhanced the acid tolerance of *L. reuteri*.

After entering the intestine, probiotics must cope with the challenges posed by ROS produced by inflammation and bile acids in the intestinal fluids. We further tested the tolerance of the modified *L. reuteri* to H_2O_2 and SIF *in vitro*. Initially, we assessed the growth of native *L. reuteri*, MnCe@LR, and MnCe@LR/AMs in SIF by measuring OD_{600} (Figure 3F). The findings demonstrated a significant enhancement in the growth rate of *L. reuteri* in SIF due to the nanozyme-microsphere modification system. After subjecting native *L. reuteri*, MnCe@LR, and MnCe@LR/AMs to incubation in SIF and H_2O_2 for a duration of 2 h, we employed plate counting after solubilization to assess their tolerance. The results demonstrated that the survival rate of MnCe@LR/AMs after SIF incubation was 19.56-fold higher compared to *L. reuteri*, and 10.88-fold higher following incubation in H_2O_2 (Figure 3G). To evaluate the impact of the nanozyme-microsphere system on *L. reuteri* growth, we plotted the growth curves of native *L. reuteri* and MnCe@LR/AMs in MRS medium without dissociation (Figure S13). After 8 h of cultivation, the *L. reuteri* population in the MnCe@LR/AMs group exhibited accelerated growth compared to the native *L. reuteri* group. This phenomenon may be attributed to the gradual swelling and subsequent structural rupture of MnCe@LR/AMs in the MRS medium (pH: 6.2–6.5), leading to the substantial release of encapsulated probiotics at the time point. After culturing native *L. reuteri* and MnCe@LR/AMs in MRS medium for 4, 8, and 12 h, plate counting results showed no significant differences between the two groups ($p > 0.05$), suggesting that the nanozyme-microsphere system did not significantly influence the survival ability of *L. reuteri* (Figure 3H).

To simulate the inflammatory colonic microenvironment in IBD patients, we supplemented the SCF with H_2O_2 at a final concentration of 5 mM. Bright-field microscopy revealed maintained structural integrity of MnCe@LR/AMs following 1 h SGF incubation, with no significant particle size alteration compared to untreated microspheres (Figure 3I,K). Zeta potential analysis demonstrated comparable characteristics pre- and post-SGF exposure, confirming gastric stability (Figure

https://doi.org/10.1021/acsnano.5c08999
ACS Nano 2025, 19, 31619–31642

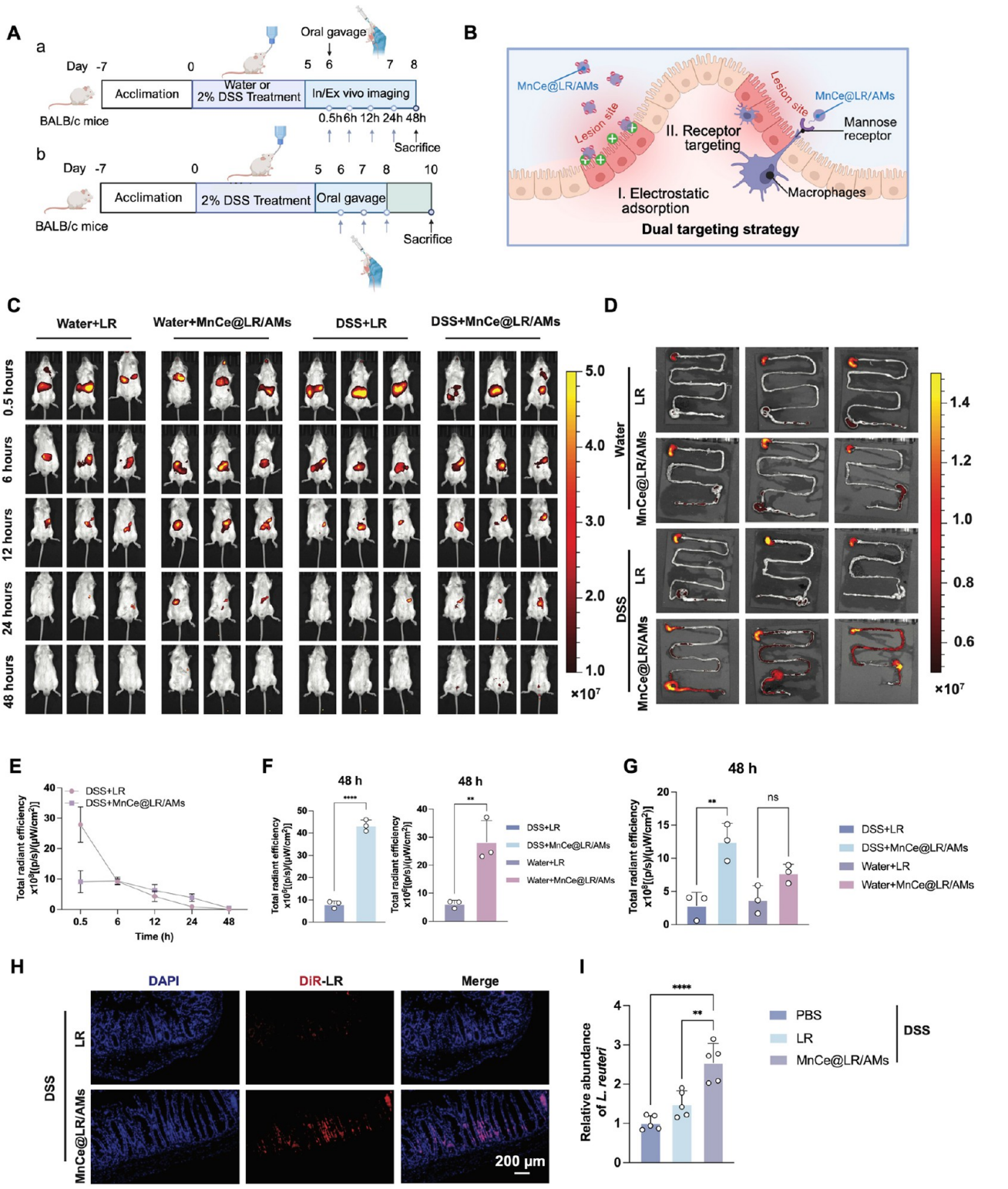

Figure 4. Enhanced Adhesion to Inflamed Mucosa by MnCe@LR/AMs. (A) Schematic diagram of the experimental schedule. Created in BioRender. Zhou, P. (2025) https://BioRender.com/xpb742i. (B) Schematic diagram of MnCe@LR/AMs targeting colonic inflammation through electrostatic adsorption and mannose receptors. Created in BioRender. Zhou, P. (2025) https://BioRender.com/kj986c0. (C) *In vivo* IVIS images at 0.5, 6, 12, 24, and 48 h after oral gavage of *L. reuteri* or MnCe@LR/AMs (1×10^8 CFU) labeled with DiR in healthy and colitis mice. (D) IVIS images of the gut at 48 h after oral gavage of LR or MnCe@LR/AMs in healthy and colitis mice. (E) Fluorescence intensity statistics of *in vivo* IVIS images at 0.5, 6, 12, 24, and 48 h after oral gavage of LR or MnCe@LR/AMs in colitis mice. (F) Fluorescence intensity statistics of *in vivo* IVIS images at 48 h after oral gavage of LR or MnCe@LR/AMs in healthy and colitis mice. (G) Fluorescence intensity statistics of intestinal tissues at 48 h after oral gavage of LR or MnCe@LR/AMs in healthy and colitis mice. (H) Fluorescence micrographs of intestinal tissue sections. (I) Relative abundance of LR in fecal samples quantified by qPCR. Data are presented as the means ± SD ($n = 3$ for (C), (D), (E), (F) and (G); $n = 5$ for (I)).

https://doi.org/10.1021/acsnano.5c08999
ACS Nano 2025, 19, 31619−31642

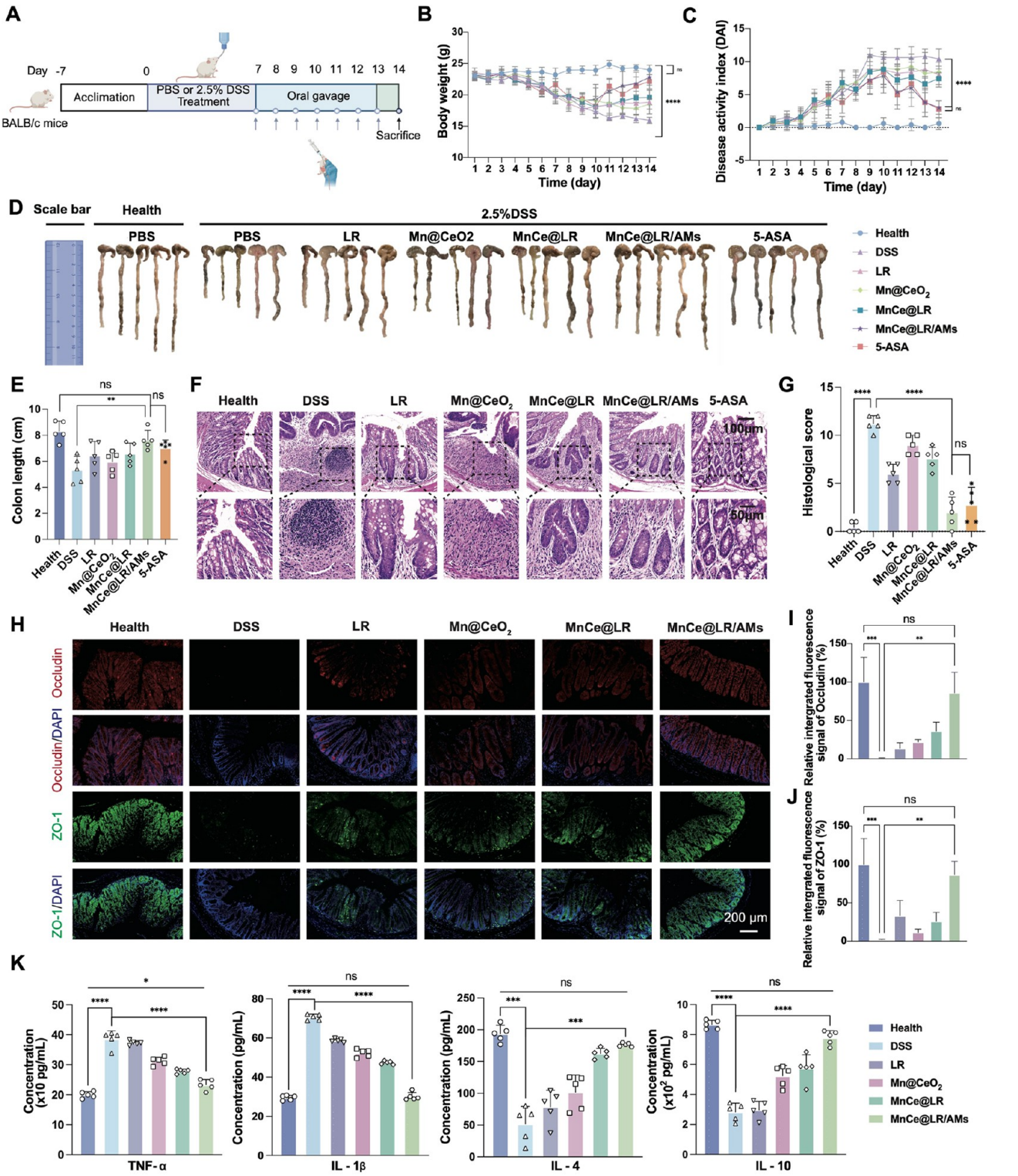

Figure 5. Therapeutic Efficacy of MnCe@LR/AMs in DSS-Induced Colitis. (A) Schematic diagram of the experimental procedure for assessing the therapeutic effect of MnCe@LR/AMs on acute colitis. After 1 week of drinking 2.5% DSS, mice developed acute colitis and were then orally administered 1×10^9 CFU of natural *L. reuteri*, $Mn@CeO_2$, MnCe@LR, or MnCe@LR/AMs for 7 consecutive days. PBS and 5-ASA were used as controls. Created in BioRender. Zhou, P. (2025) https://BioRender.com/xpb742i. (B) Body weight changes during the 14-day period of colitis induction and treatment. (C) Daily changes in DAI scores for each group. (D) Digital images of cecal-colon tissues collected after euthanasia for each group. (E) Colon length measurements for each group post-treatment. (F) Representative H&E-stained images of colon tissues for each group. Scale bar: 100 and 50 μm. (G) Histopathological scores of colon tissues for each group. (H) Representative immunofluorescence images of ZO-1 and occludin in colon tissues for each group. Scale bar: 200 μm. (I) Statistical analysis of relative integrated fluorescence signal of occludin immunofluorescence images in colon tissues for each group. (J) Statistical analysis of relative integrated fluorescence signal of ZO-1 immunofluorescence images in colon tissues for each group. (K) Concentrations of TNF-α, IL-1β, IL-4, and IL-10 in mouse serum measured using an ELISA kit. Data are presented as the means ± SD (n = 5 for (B), (C), (E), (G) and (K); n = 3 for (I) and (J)).

https://doi.org/10.1021/acsnano.5c08999
ACS Nano 2025, 19, 31619−31642

3J). Conversely, SCF incubation induced substantial structural disintegration, rendering size quantification impractical (Figure 3I). The observed zeta potential shift (−5.753 mV to −24.13 mV) likely originated from increased surface area and exposed carboxyl groups of alginate fragments postdisintegration, rather than enhanced stability. These results collectively demonstrate MnCe@LR/AMs' gastric stability and colon-responsive disintegration. In conclusion, the nanozyme-microsphere system demonstrated excellent probiotic protection in a harsh gastrointestinal environment.

Enhanced Adhesion to Inflamed Mucosa by MnCe@LR/AMs. After passing through the upper gastrointestinal tract, probiotics must remain in the intestine for a prolonged period to enhance their therapeutic effects. Therefore, we labeled *L. reuteri* and MnCe@LR/AMs with DiR to verify whether the nanozyme-hydrogel microsphere system could improve the mucosal adhesion ability of *L. reuteri* in the mouse intestine. First, a colitis model was created by providing free dextran sodium sulfate (DSS) solution for 5 days, followed by oral administration of 1×10^8 CFU of LR or MnCe@LR/AMs. Fluorescence signals from DiR-LR were detected at different time points utilizing the *in vivo* imaging system (IVIS) to analyze the distribution and intestinal retention of DiR-LR. All groups of mice were euthanized at the 48 h time point, and their colons were extracted for fluorescence imaging (Figure 4A (a)). By measuring the IVIS fluorescence intensity, we assessed the retention time and biodistribution of LR and MnCe@LR/AMs in healthy and inflamed colons. Following oral gavage of free DiR, fluorescence signals in mice became nearly undetectable after 12 h (Figure S14). After accounting for potential dye retention effects, DSS-induced model mice demonstrated distinct fluorescence patterns: while initial signals were stronger in LR-gavaged mice compared to MnCe@LR/AMs-treated mice, the MnCe@LR/AMs group exhibited significantly superior fluorescence intensity after 12 h (Figure 4C, E and F). Similarly, MnCe@LR/AMs showed prolonged intestinal retention in healthy mice (Figure 4C,F). Fluorescence imaging of intestinal tissues 48 h postgavage revealed significantly stronger signal intensity in both experimental groups receiving MnCe@LR/AMs compared to LR (Figure 4D,G). This indicated that the nanozyme-microsphere system effectively enhanced the adhesion capability in both normal and inflamed intestines, prolonging the persistence of probiotics in the intestine.

Severe damage to the mucosal layer can greatly affect probiotic adhesion and colonization. The negatively charged alginate microspheres helped retain the probiotics in the inflamed colon region, achieving targeted delivery to the inflamed colon area (Figure 4B). Therefore, we investigated whether MnCe@LR/AMs could enhance the adhesion and targeting of *L. reuteri* in an inflamed intestinal environment. Colitis was induced in mice via 2% DSS in drinking water for 5 days. Following induction, mice were treated with PBS, 1×10^8 CFU of DiR-labeled LR, or MnCe@LR/AMs via daily oral gavage for 3 days. Tissues and intestinal contents were harvested 48 h post-treatment for further analysis (Figure 4A(b)). Fluorescence imaging of intestinal tissue sections revealed higher LR colonization in MnCe@LR/AMs-treated mice compared to free LR administration (Figure 4H). Subsequent qPCR analysis of fecal DNA demonstrated a significantly higher relative abundance of LR in the MnCe@LR/AMs group ($p = 0.0013$) (Figure 4I), confirming the enhanced microbial retention capability of the nanozyme-microsphere system. In conclusion, the nanozyme-microsphere system significantly enhanced the attachment and persistence of probiotics in the inflamed colon area, further demonstrating its potential for improving probiotic-based treatments for IBD.

Therapeutic Efficacy of MnCe@LR/AMs in DSS-Induced Colitis. After confirming that the nanozyme-microsphere system could improve probiotic tolerance to the harsh gastrointestinal environment and enhance delivery to the intestinal inflammatory area, we further explored the potential of MnCe@LR/AMs as a treatment for ulcerative colitis. Therefore, we chose the acute colitis mouse model induced by DSS for the following *in vivo* experiments.[29] The model-construction process is illustrated in Figure 5A. After a week of adaptation feeding, the mice were continuously administered 2.5% DSS solution for 7 days to induce acute colitis and then gavaged daily with MnCe@LR/AMs containing 1×10^9 CFU of *L. reuteri* for 7 days. Natural *L. reuteri*, Mn@CeO_2, MnCe@LR, 5-ASA (an anti-inflammatory drug often used in the treatment of IBD), and PBS were used as control groups.

Throughout the 14-day treatment period, body weight, stool consistency, and occult blood changes were monitored, and disease activity index (DAI) scores were calculated from these data. The results revealed that mice in the MnCe@LR/AMs group had the fastest weight recovery, without any significant difference when compared to the 5-ASA group (Figure 5B). Although *L. reuteri*, Mn@CeO_2, and MnCe@LR alleviated weight loss to some extent, their effects were not as pronounced as those of MnCe@LR/AMs. Weight loss was not prevented in the mice in the DSS group. In line with this, the DAI scores indicated that the MnCe@LR/AMs intervention group showed the most significant reduction in disease activity, which was close to the effect of the commonly used IBD treatment drug 5-ASA (Figure 5C). Furthermore, the colon length in the DSS group was notably reduced, while in the MnCe@LR/AMs treatment group, it was similar to that in the Health group (Figure 5D,E). DSS-induced colitis is usually accompanied by the infiltration of inflammatory cells and damage to epithelial cells.[30] Therefore, we assessed the degree of colon damage through histopathological scoring (Table S1). Representative H&E stained images and scoring results indicated that MnCe@LR/AMs treatment markedly alleviated the intestinal damage induced by DSS, demonstrating a strong anti-inflammatory effect (Figure 5F,G). AB-PAS staining analysis revealed a significant increase in goblet cells per crypt length in the MnCe@LR/AMs-treated group compared to the DSS group, reaching levels comparable to the Health group, which further validates the beneficial effects of MnCe@LR/AMs on intestinal barrier function restoration (Figure S15).

During colonic inflammation, the intestinal barrier integrity is significantly impaired. To evaluate the recovery of the intestinal barrier, we measured the expression of tight junction proteins (ZO-1 and occludin) in the intestines of each group. Immunofluorescence results and semiquantitative analysis showed that MnCe@LR/AMs significantly restored the expression of ZO-1 and occludin to levels comparable to those in normal intestinal tissues (Figure 5H–J). We performed additional Western blot experiments to validate the expression changes of ZO-1 and occludin. Semiquantitative analysis revealed significantly elevated ZO-1 expression in the colonic tissues of MnCe@LR/AMs-treated mice compared to the DSS group, reaching levels comparable to the health group. A similar expression pattern was observed for occludin (Figure S16). Furthermore, we measured the concentrations of pro-inflam-

https://doi.org/10.1021/acsnano.5c08999
ACS Nano 2025, 19, 31619−31642

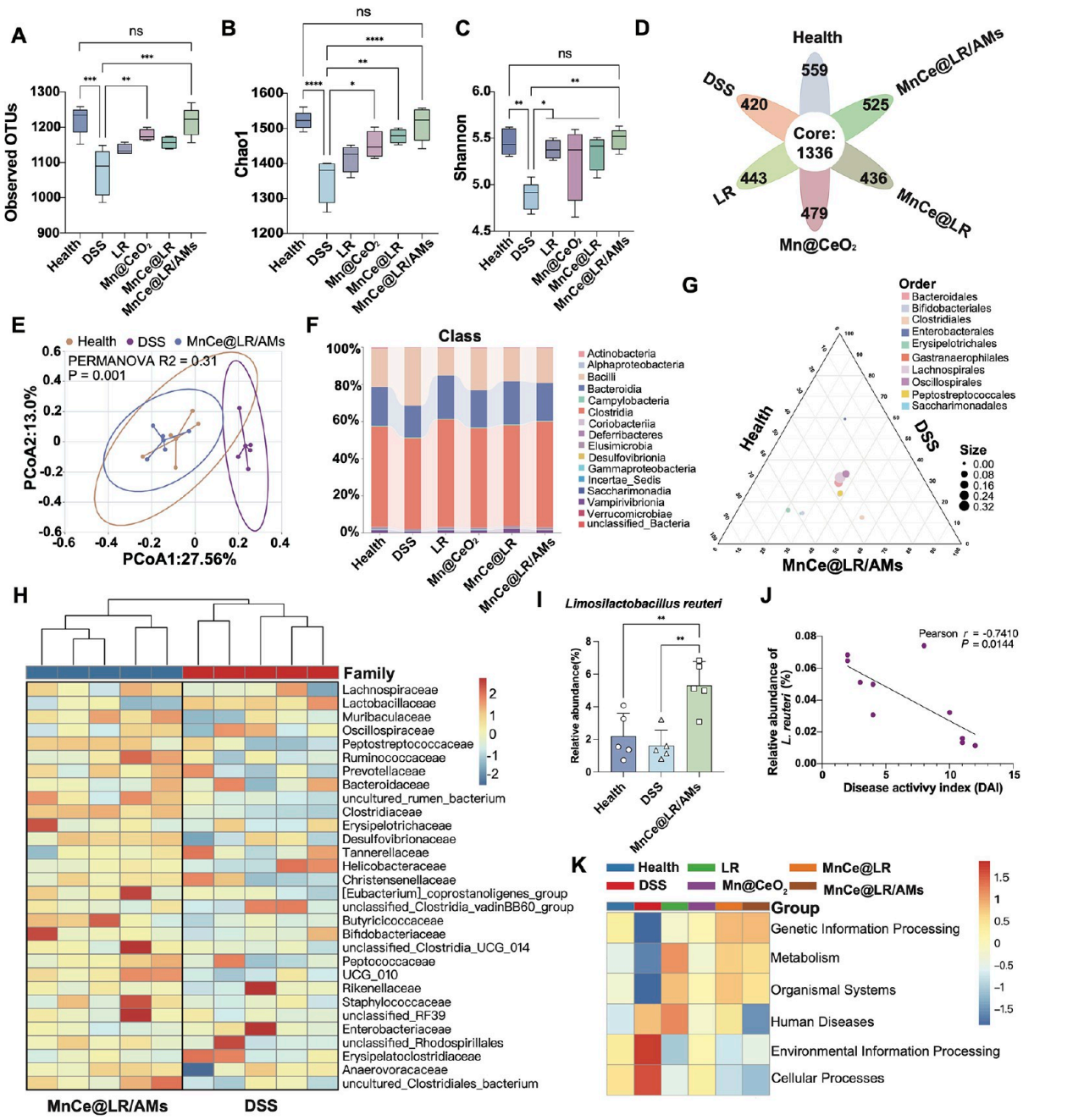

Figure 6. Regulatory Effects of MnCe@LR/AMs on Gut Microbiota in Mice with Acute Colitis. Comparison of α-diversity between groups using (A) species count, (B) Chao1 index, (C) Shannon index, and (D) number of characteristic species presented in a petal chart. (E) PCoA plot based on Weighted Unifrac distance for clustering the gut microbiota of the Health, DSS, and MnCe@LR/AMs groups. (F) Stacked bar chart showing the relative abundance of gut microbiota at the class level. (G) Ternary plot illustrating the impact of MnCe@LR/AMs on the microbiota composition at the order level. (H) Heatmap comparing the relative abundance of gut microbiota at the family level between the DSS and MnCe@LR/AMs groups. (I) Comparison of relative abundance of *L. reuteri* between the Health, DSS, and MnCe@LR/AMs groups. (J) Linear regression plots and Pearson correlation analysis of DAI and relative abundance of *L. reuteri* in DSS and MnCe@LR/AMs groups on day 14. (K) Heatmap of functional predictions of the gut microbiota in each group based on KEGG pathways. Data are presented as the means ± SD (n = 5).

matory and anti-inflammatory cytokines in the serum, including TNF-α, IL-1β, IL-4, and IL-10, using ELISA. MnCe@LR/AMs reduced the excretion of pro-inflammatory cytokines (TNF-α and IL-1β), while increasing the secretion of anti-inflammatory cytokines (IL-4 and IL-10) (Figure 5K). In conclusion, MnCe@LR/AMs exhibited excellent therapeutic effects in the DSS-induced acute colitis model, significantly alleviating intestinal inflammation and rebuilding intestinal barrier function.

Regulatory Effects of MnCe@LR/AMs on Gut Microbiota in Mice with Acute Colitis. Recent evidence reveals that remodeling the intestinal flora balance is a pivotal strategy for IBD treatment.[31] After confirming that MnCe@LR/AMs displayed considerable therapeutic efficacy against acute colitis in mice, we investigated whether MnCe@LR/AMs could remodel the gut microbiota to enhance treatment efficacy. Therefore, we conducted 16S rDNA amplicon sequencing of

https://doi.org/10.1021/acsnano.5c08999
ACS Nano 2025, 19, 31619−31642

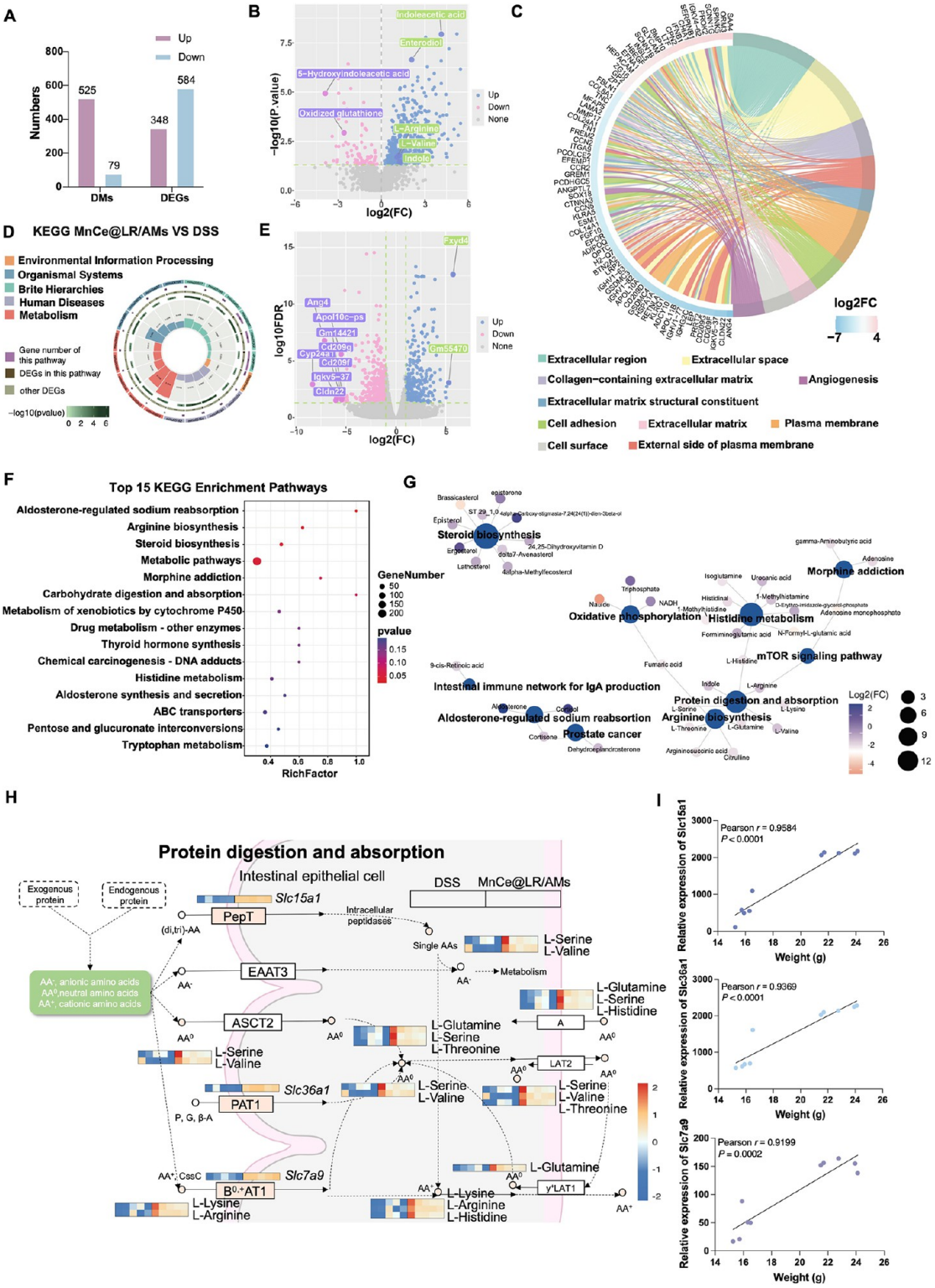

Figure 7. The Combined Metabolomic and Transcriptomic Analysis of MnCe@LR/AMs in the Treatment of Acute Colitis. (A) Bar chart showing the number of DEGs and DMs in the MnCe@LR/AMs group compared to the DSS group. (B) Volcano plot of DMs between the MnCe@LR/AMs group and the DSS group. (C) GO-based pathway enrichment chord diagram for DEGs in the MnCe@LR/AMs group compared to the DSS group. (D) KEGG-based pathway enrichment circular diagram for DEGs in the MnCe@LR/AMs group compared to the DSS group. (E) Volcano plot of DEGs between the MnCe@LR/AMs group and the DSS group. (F) KEGG-based pathway enrichment bubble chart for DMs in the MnCe@LR/AMs group compared to the DSS group. (G) Network diagram of differentially modified metabolites and enriched pathways. (H) Schematic diagram showing key gene and metabolite changes in the protein digestion and absorption pathways between the MnCe@LR/AMs and DSS groups. Created in BioRender. Zhou, P. (2025) https://BioRender.com/nbrcaff. (I) Linear regression plots and Pearson correlation analysis of body weight and relative expression of *Slc7a9*, *Slc15a1* and *Slc36a1* in DSS and MnCe@LR/AMs groups on day 14. Data are presented as the means ± SD (n = 5).

https://doi.org/10.1021/acsnano.5c08999
ACS Nano 2025, 19, 31619−31642

fecal samples from all groups of mice to assess the impact of different treatments on the gut microbiota in mice. Species annotation was performed using the classify-sklearn algorithm in QIIME 2, and community abundance was analyzed at various taxonomic levels to assess microbiota richness and diversity. Earlier research has demonstrated that greater microbial diversity is linked to better health outcomes,[32] whereas DSS-induced colitis typically leads to decreased microbial diversity and abundance.[33] We analyzed the α-diversity of each group, including the Chao1 index, Shannon index, and observed the species count. The results indicated that, compared to other treatment groups, the MnCe@LR/AMs-treated group displayed a significant increase in species count, Chao1 index, and Shannon index (Figure 6A−D), indicating that MnCe@LR/AMs significantly restored the α-diversity of colitis mice. To further analyze the species diversity differences among the groups, we performed a β-diversity assessment and compared the microbiota diversity of the Health, DSS, and MnCe@LR/AMs groups using principal coordinate analysis (PCoA) (Figure 6E). Dimensionality reduction using the Bray−Curtis distance algorithm revealed that the microbial composition of the MnCe@LR/AMs group showed a significant difference compared to that of the DSS group and closer to that of the Health group. PERMANOVA testing (p = 0.001) confirmed that there were notable variations in the microbial composition, further demonstrating that the MnCe@LR/AMs-treated group restored a gut microbiota structure resembling that of the Health group.

The stacked bar plot of the bacterial abundance at the class level (Figure 6F) shows the effects of the different treatments on the mouse gut microbiota. Research has indicated that the abundance of *Bacteroidia* is diminished in individuals with IBD.[34] *Clostridia* are important symbiotic bacteria that exert anti-inflammatory effects by fermenting fiber in the diet to generate short-chain fatty acids.[35] After supplementation with MnCe@LR/AMs, the relative abundances of both *Bacteroidia* and *Clostridia* were significantly restored. At the order level, ternary plot analysis indicated that MnCe@LR/AMs significantly restored the abundance of *Bifidobacteriales* (which help improve IBD symptoms and enhance gut barrier function),[36] *Clostridiales* (which regulate immune responses and gut health by producing short-chain fatty acids),[35] *Gastranaerophilales* (associated with the improvement of DSS-induced colitis),[37] and *Peptostreptococcales_Tissierellales* (with potential for short-chain fatty acid production),[38] while significantly reducing the abundance of *Enterobacterales* (including pathogenic bacteria such as *Escherichia coli* and *Salmonella*, which exacerbate intestinal inflammation)[39] (Figure 6G). Heatmaps at the family level show that MnCe@LR/AMs substantially increased the presence of beneficial bacteria, such as *Ruminococcaceae, [Eubacterium] coprostanoligenes_group, Bifidobacteriaceae, Peptococcaceae,* and others, while decreasing the abundance of *Enterobacteriaceae*, which are associated with IBD (Figure 6H). At the genus and species levels, after intervention with MnCe@LR/AMs, the abundance of probiotics such as *Limosilactobacillus, NK4A214_group, Lachnospiraceae_NK4A136_group,* and *Akkermansia* was significantly restored, whereas the concentration of harmful bacteria such as *Escherichia_Shigella* was reduced to levels comparable to those in healthy mice (Figure S17). Species-level analysis showed that the abundance of probiotics, such as *L. reuteri*, *Akkermansia muciniphila*, and *Lactobacillus intestinalis* increased, whereas that of pathogenic bacteria, such as *E. coli* and *Enterococcus hirae* decreased (Figures 6I and S18). The correlation analysis (Figure 6J) reveals a notable negative correlation between the relative abundance of *L. reuteri* and the DAI in colitis mice (r = −0.7410, p = 0.014), further supporting the therapeutic potential of *L. reuteri* for colitis. Linear discriminant analysis showed the distribution of dominant and characteristic bacterial populations across various taxonomic levels (Figure S19). Finally, we used Tax4Fun2 to predict the functional characteristics of the microbiota in each group (Figure 6K). The heatmap shows that MnCe@LR/AMs treatment significantly restored metabolic dysfunction in the gut microbiota and reduced disease-related enrichment. Overall, these data strongly demonstrate that MnCe@LR/AMs can significantly relieve DSS-induced colitis symptoms through modulation of microbiota dysbiosis in mice with colitis.

The Combined Metabolomic and Transcriptomic Analysis of MnCe@LR/AMs in Treating Acute Colitis. To further elucidate the therapeutic mechanism of MnCe@LR/AMs, we compared the metabolomic and transcriptomic data of the DSS and MnCe@LR/AMs groups and performed a combined analysis. Metabolomic analysis revealed that compared to the DSS group, 525 metabolites were upregulated and 79 were downregulated in the MnCe@LR/AMs group, whereas 348 genes were upregulated and 584 were downregulated (Figure 7A). Principal component analysis (PCA) shows a significant difference in the metabolite composition between the two groups (Figure S20). Volcano plots (Figure 7B) further illustrate the differential metabolites (DMs): in the MnCe@LR/AMs group, tryptophan metabolites (such as indole-3-acetic acid and indole) and amino acids (such as L-arginine and L-valine) were significantly elevated, which help regulate intestinal homeostasis and the immune system, alleviating inflammation.[40] Meanwhile, 5-hydroxyindoleacetic acid (a tryptophan metabolite associated with gut dysfunction)[41] and oxidized glutathione (a metabolite reflecting cellular stress and antioxidant levels)[42] were significantly reduced in the MnCe@LR/AMs group, suggesting that its antioxidant effect may be more potent.

Transcriptome analysis revealed significant changes in gene expression in the MnCe@LR/AMs group (Figure 7E). KEGG pathway enrichment analysis indicated that these differentially expressed genes (DEGs) were highly associated with metabolic processes (Figure 7D). Additionally, GO enrichment analysis showed that the differentially expressed genes in the MnCe@LR/AMs intervention group were enriched in multiple immune and microbiota regulation pathways, such as the extracellular region, cell adhesion, innate immune response, and bacterial response (Figure 7C). The enrichment of these pathways underscores the significant regulatory effects of MnCe@LR/AMs on the immune system and microbiota. In the KEGG enrichment analysis of differential metabolites (Figure 7F), amino acid metabolism pathways (such as arginine, histidine, and tryptophan) were notably significant. Further network analysis revealed that the upregulated amino acid metabolites in the MnCe@LR/AMs group play a key role in protein digestion and absorption pathways (Figure 7G).

Subsequently, we performed a combined analysis of differential metabolites and genes using O2PLS analysis and intergroup correlation heat maps (Figures S21 and S22),[43] revealing that MnCe@LR/AMs significantly improved protein digestion and absorption in the gut. The heatmap of this pathway shows that compared to the DSS group, genes such as *Slc15a1*, *Slc36a1*, and *Slc7a9* were significantly upregulated in the MnCe@LR/AMs group (Figure 7H). *Slc15a1* regulates the

https://doi.org/10.1021/acsnano.5c08999
ACS Nano 2025, 19, 31619−31642

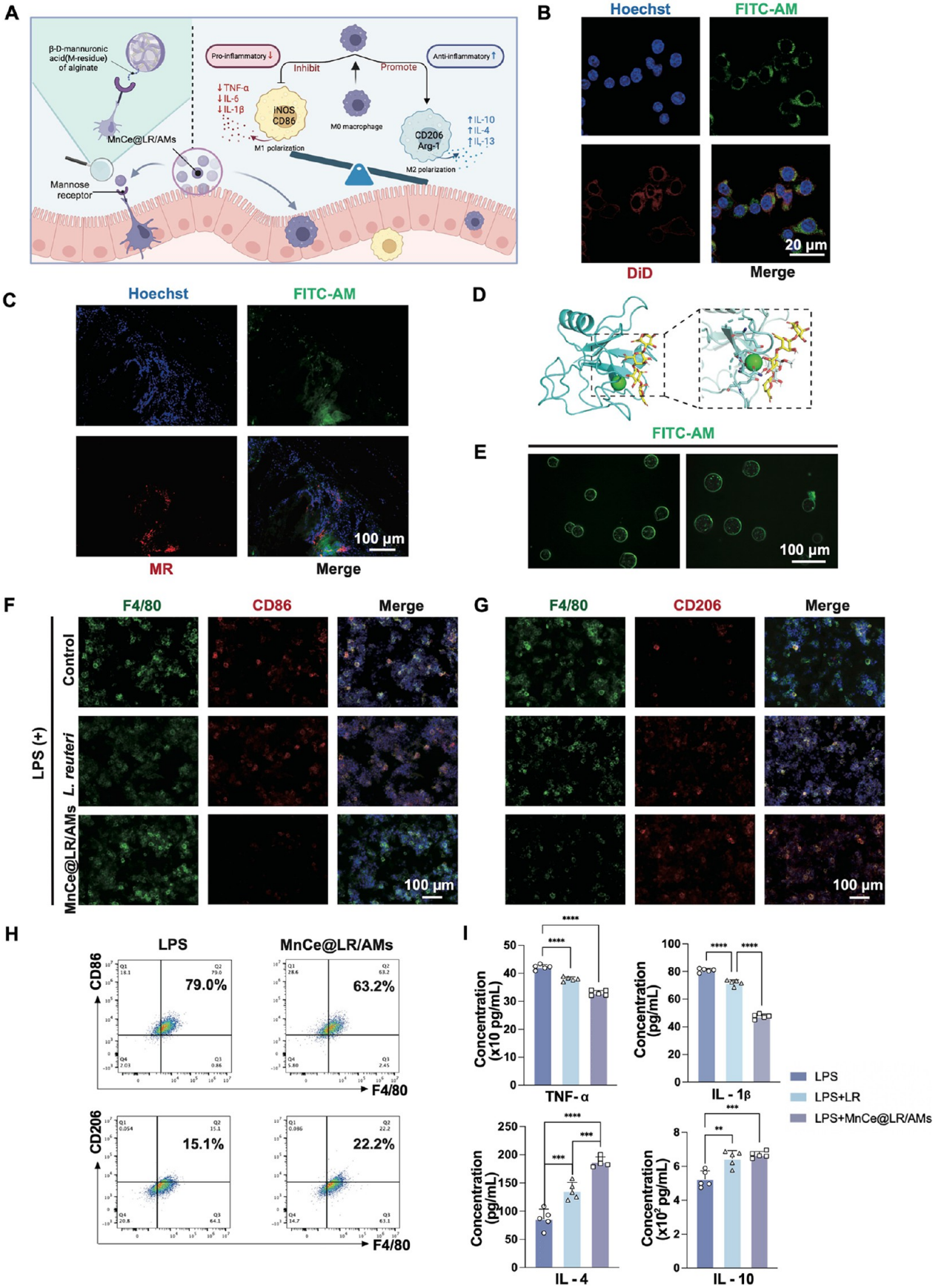

Figure 8. ***In vitro*** **immunomodulatory activity of MnCe@LR/AMs. (A) Schematic diagram illustrating the role of MnCe@LR/AMs in improving colonic inflammation by modulating macrophage polarization. Created in BioRender. Zhou, P. (2025) https://BioRender.com/w2hgww5. (B) Fluorescence confocal images of MnCe@LR/AMs coincubated with RAW264.7 cells. The green channel represents FITC-labeled AM, and the**

https://doi.org/10.1021/acsnano.5c08999
ACS Nano 2025, 19, 31619−31642

Figure 8. continued

red channel represents DiD-labeled cell membranes. Scale bar: 20 μm. (C) Immunofluorescence images of intestinal tissue in colitis mice after intervention with MnCe@LR/AMs. The green channel represents FITC-labeled AM. The red channel represents MR. Scale bar: 100 μm. (D) The binding pose of MMGM alginate fragment with mannose receptor. (E) Fluorescence images of FITC-AM Labeled MnCe@LR/AMs. Scale bar: 100 μm. (F) Immunofluorescence staining of F4/80 and CD86 in LPS-induced macrophages after coincubation with *L. reuteri* or MnCe@LR/AMs for 24 h. The red channel represents CD86, and the green channel represents F4/80. Scale bar: 100 μm. (G) Immunofluorescence staining of F4/80 and CD206 in LPS-induced macrophages after coincubation with *L. reuteri* or MnCe@LR/AMs for 24 h. The red channel represents CD206, and the green channel represents F4/80. Scale bar: 100 μm. (H) Representative images of surface markers on LPS-induced RAW264.7 cells after intervention with MnCe@LR/AMs, analyzed by flow cytometry. (I) ELISA detection of TNF-α, IL-1β, IL-4, and IL-10 expression in the supernatant of LPS-induced RAW264.7 cells after 24 h intervention with *L. reuteri* or MnCe@LR/AMs. Data are presented as the means ± SD (n = 5 for (I)).

expression of the neutral amino acid transporter PepT1, *Slc36a1* regulates the expression of the proline/glycine transporter PAT1, and *Slc7a9* regulates the expression of the cationic amino acid transporter $B^{0,+}AT1$. Correspondingly, neutral (e.g., serine) and cationic (e.g., arginine) amino acids were significantly more abundant in the MnCe@LR/AMs group. The abundance of amino acids in the gut is crucial for the immune system because they can activate macrophage activity, promote antigen clearance, and stimulate immune responses.[44] Additionally, amino acids, as precursors of protein synthesis, help accelerate tissue regeneration and healing, thereby reducing disease duration and shortening recovery time.[45] We performed a Pearson correlation analysis between the body weight of colitis mice after 7 days of intervention and the relative abundance of intestinal amino acids and peptide transporter-regulating genes (Figures 7I and S23). A significant positive correlation was observed, suggesting that MnCe@LR/AMs may help prevent continued weight loss by improving protein absorption in the gut.

***In Vitro* Immunomodulatory Activity of MnCe@LR/AMs.** Previous research has revealed that the functional state of macrophages is vital in IBD,[46] and regulating their polarization status could be a new strategy for IBD treatment. Based on the transcriptomic analysis showing the immunomodulatory effects of MnCe@LR/AMs, we performed immune infiltration analysis and discovered that MnCe@LR/AMs might exert immune modulation through macrophages (Figure S24). Therefore, we hypothesized that MnCe@LR/AMs modulate the immune response by influencing macrophage polarization (Figure 8A). To verify whether MnCe@LR/AMs could be internalized, we labeled alginate microsphere (AM) with FITC and observed their uptake by RAW264.7 macrophages (Figure 8E). Fluorescence microscopy showed green fluorescence within the cytoplasm, demonstrating successful internalization of MnCe@LR/AMs—though not in their intact microsphere form. We propose that MnCe@LR/AMs dissociated into smaller subunits about 1 h after being introduced into DMEM medium (pH 7.2−7.4), subsequently undergoing endocytosis by macrophages (Figures 8B and S25). Confocal fluorescence imaging confirmed the macrophage-mediated endocytosis of *L. reuteri*, $Mn@CeO_2$ and alginate microsphere by 2 h post-exposure (Figures 8B and S26A).

Subsequently, the M1 macrophage phenotype was induced by 100 ng/μL LPS treatment, and macrophage populations were labeled with F4/80. M1 and M2 macrophages were identified using CD86 and CD206, respectively. Cell immunofluorescence staining and quantification showed that CD86 fluorescence in the MnCe@LR/AMs group was significantly reduced compared to the other groups, while CD206 fluorescence was notably increased (Figure 8F,G), suggesting that MnCe@LR/AMs induced the macrophage polarization toward the M2 phenotype and inhibited M1 polarization. Flow cytometry analysis of CD86 and CD206 expression in RAW264.7 cells revealed a significant reduction in the percentage of CD86-positive cells in the MnCe@LR/AMs treatment group (79% in the LPS group vs 63.2% in the MnCe@LR/AMs group), while the percentage of CD206-positive cells increased significantly (15.1% in the LPS group vs 22.2% in the MnCe@LR/AMs group) (Figure 8H). Flow cytometry analysis of colonic lamina propria cells from the DSS group, LR group, and MnCe@LR/AMs group mice demonstrated that MnCe@LR/AMs treatment significantly reduced the proportion of M1 macrophages while increasing M2 macrophage population compared to both DSS and LR groups, thereby confirming its *in vivo* capacity to modulate macrophage polarization (Figure S27). Additionally, ELISA results indicated that, compared to the control group, the levels of pro-inflammatory cytokines TNF-α and IL-1β were significantly reduced, whereas the levels of anti-inflammatory cytokines IL-4 and IL-10 were significantly elevated in the MnCe@LR/AMs treatment group (Figure 8I). In conclusion, MnCe@LR/AMs effectively modulated macrophage polarization under inflammatory conditions, thereby exerting a positive effect on inflammation suppression and immune regulation.

We further investigated the mechanism by which MnCe@LR/AMs target macrophages. A study by Huang et al. revealed that the β-D-mannuronic acid residues of SA can bind to the MR on antigen-presenting cell membranes, enabling targeting to the inflammatory region.[20] MRs are also present on the surface of macrophages, leading us to hypothesize that MnCe@LR/AMs achieve a "dual-targeting" effect by targeting the MRs on macrophage surfaces. Previous studies have confirmed that MR is highly expressed at sites of inflammation.[47,48] Molecular docking simulations confirm that MMGM alginate fragments bind to MR with a binding energy of −5.3 kcal/mol, which is lower than that of the original ligand (−5 kcal/mol). This suggests that sodium alginate exhibits stronger spontaneous binding to MR when in a polymeric state (Figures 8D and S28). We further performed MM/PBSA calculations to compare the binding abilities of the original ligand (methyl-mannoside) and monomer-based alginate (mannopyranuronic acid) with MR. The results showed that the binding energy for methyl-mannoside transitioning from the free to bound state was −9.6876 kcal/mol, while that for mannopyranuronic acid was −7.6486 kcal/mol. Although slightly lower than the original ligand, the binding energy of −7.6486 kcal/mol indicates that mannopyranuronic acid binds effectively to MR, with binding ability only slightly weaker than the original ligand (Tables S2 and S3).

Furthermore, we conducted *in vivo* experiments to validate the MR-targeting capability of MnCe@LR/AMs. Following 7-

https://doi.org/10.1021/acsnano.5c08999
ACS Nano 2025, 19, 31619−31642

day DSS-induced colitis modeling, DSS mice received MnCe@LR/AMs via oral gavage and were euthanized 12 h postadministration for intestinal specimen collection and immunofluorescence staining. Immunofluorescence imaging revealed specific targeting affinity of MnCe@LR/AMs toward MR (Figure 8C). Competitive inhibition of the MR on macrophages by the addition of mannose significantly reduced the uptake of LR by macrophages (Figure S26B,C). These experiments confirmed our hypothesis that MnCe@LR/AMs can not only attract macrophages through charge interaction, but also achieve dual-targeting through alginate-MR binding, specifically localizing to the inflammation site.

Therapeutic Efficacy of MnCe@Lr/AMs in TNBS-Induced Crohn's Disease (CD). After confirming the therapeutic effect of MnCe@LR/AMs in the DSS-induced colitis model, we evaluated the therapeutic effectiveness of MnCe@LR/AMs in a TNBS-induced CD mouse model (Figure S29A).[49] As anticipated, compared with the other treatment groups, MnCe@LR/AMs significantly improved body weight recovery and effectively reduced the DAI score (Figure S29B,C). The TNBS-induced CD mice exhibited significant shortening of the colon length, whereas the MnCe@LR/AMs group showed a significant recovery in colon length, with no significant difference compared to the Health group (Figure S29D,E). Taken together, MnCe@LR/AMs exhibited excellent therapeutic effects in a TNBS-induced model of CD, further confirming their therapeutic potential in CD.

Biosafety of MnCe@LR/AMs. The biocompatibility of MnCe@LR/AMs was evaluated using *in vivo* oral administration experiments. After grouping healthy mice, they were orally gavaged with either PBS or MnCe@LR/AMs and analyzed 7 days later, after euthanasia (Figure S30A). As expected, no significant body weight loss was observed in the MnCe@LR/AM-treated mice in comparison with the Health group (Figure S30B). Additionally, histological analysis of the major organs revealed no significant differences in the tissue structures of the heart, liver, spleen, lungs, or kidneys between the MnCe@LR/AM-treated and untreated groups (Figure S30C). These results indicate that MnCe@LR/AMs exhibit excellent biocompatibility with negligible side effects.

DISCUSSION

Intestinal microbiota therapy has become a significant focus in the research and management of IBD and other gastrointestinal conditions with broad application prospects.[50] However, the low tolerance of the gut microbiota to digestive fluids and their short retention time in the intestines results in low probiotic utilization and insufficient duration of action, which limits their further clinical application.[51] Previous studies have shown that simple probiotic−antioxidant systems significantly enhance the ROS-scavenging ability of probiotics but suffer from insufficient targeting capability. Hydrogel systems can protect probiotics and increase their colonization rate but are less effective in mitigating oxidative stress. Therefore, there is an urgent need to develop functional, highly targeted, protective, and biocompatible probiotic delivery systems. To fill these gaps, we developed a probiotic delivery system based on nanozymes and SA microspheres (MnCe@LR/AMs; Scheme 1 and Figure 1).

Metal doping in nanozymes represents a well-established strategy for enhancing catalytic activity. Recent studies have demonstrated that incorporating Cu/Pt bimetallic sites into CeO_2 to construct $PtCuO_x/CeO_{2-x}$ nanozymes can effectively increase oxygen vacancy concentration and modulate the Ce^{3+}/Ce^{4+} ratio, thereby synergistically improving both SOD-like and CAT-like activities.[52] In this study, Mn-doped CeO_2 was developed to enhance the Ce^{4+}/Ce^{3+} ratio and increase oxygen vacancy concentration, thereby significantly improving ROS scavenging capacity. The increased Ce^{4+} ratio and oxygen vacancies enhance SOD-like and catalase-like activities through three mechanisms: The Ce^{4+}/Ce^{3+} redox equilibrium promotes catalytic efficiency, as higher Ce^{4+} content directly improves CAT-like activity;[53] Mn doping in $Mn@CeO_2$ alters the electronic structure, facilitating electron transfer during ROS scavenging;[54] Oxygen vacancies provide additional active sites, improving adsorption and decomposition of H_2O_2 and $O_2^{\cdot-}$.[55]

The absence of targeting limits the effectiveness of probiotics in IBD therapy. Prioritizing adhesion to inflamed sites offers a promising delivery strategy.[11] Utilizing the principle of electrostatic adsorption to design novel drugs for targeted delivery to positively charged intestinal inflammatory sites is a common strategy.[13] However, we aim to develop a dual-targeting system that further enhances delivery precision through ligand−receptor binding interactions. Research indicates that antigens like CD44 and MR are overexpressed at intestinal inflammation sites.[48] To address this, we designed alginate microspheres that use the M groups in alginate for spontaneous binding with MR, ensuring precise delivery of *L. reuteri* to inflamed areas. Molecular docking and MM/PBSA results confirm our hypothesis: alginate forms stable bonds with calcium via hydroxyl groups, and MMGM alginate demonstrates stronger binding than the original ligand. MR possesses multiple carbohydrate-binding domains (CBDs) with a flexible 4.8 nm spacing, protruding significantly from the cell surface, which enhances its binding to alginate.[56] Furthermore, studies indicate that carbohydrate-based materials can induce MR clustering,[57] supporting the rationale for enhanced alginate-MR binding.

Conventional therapeutic agents employed for the management of ulcerative colitis, including anti-inflammatory medications, immunosuppressants, and biologics, have demonstrated the potential to disturb the gut microbiota and induce alterations in microbial proportions.[58] In contrast, owing to the involvement of probiotics, MnCe@LR/AMs not only achieved significant therapeutic effects but also improved the gut microbiota diversity in colitis mice, remodeling the microbial composition (Figure 6). Additionally, SA, an indigestible carbohydrate, can be partially metabolized by specific bacteria into short-chain fatty acids,[59] which have extensive regulatory effects on the host immune system, intestinal barrier function, and microbiota balance, helping alleviate intestinal inflammation and maintain gut health.[60] Previous studies have found that the abundances of *Bifidobacteria* and *Lactobacilli* are typically reduced in the intestines of patients with IBD.[61] As important fermentative gut microbes, *Bifidobacteria*, *Lactobacilli*, and some *Clostridia* are essential for short-chain fatty acid metabolism.[62] Our study demonstrated that MnCe@LR/AMs treatment notably enhanced the abundance of these fermentative bacteria in mice, playing an essential role in maintaining intestinal homeostasis.

Following the confirmation of MnCe@LR/AMs' therapeutic efficacy against colonic inflammation, we explored the gene transcription and metabolic changes in the intestines of mice with colitis after MnCe@LR/AMs treatment (Figure 7). The results showed that MnCe@LR/AMs intervention significantly increased the abundance of beneficial metabolites, such as tryptophan and amino acids, while downregulating the

https://doi.org/10.1021/acsnano.5c08999
ACS Nano 2025, 19, 31619−31642

abundance of oxidative markers (oxidized glutathione), suggesting that MnCe@LR/AMs improved intestinal metabolism and exhibited antioxidant effects. After conducting a combined analysis of differential metabolites and genes, we found that MnCe@LR/AMs treatment activated protein digestion and absorption, improved amino acid metabolism in the intestine, thereby enhancing nutrient absorption and alleviating weight loss in colitis mice. Research indicates significant abnormalities in amino acid metabolism and absorption in IBD patients, resulting in amino acid depletion and malnutrition. In active CD patients, serum concentrations of aromatic amino acids, including L-phenylalanine and L-tryptophan are notably lower.[63] Therefore, we propose that the observed improvement in protein absorption mediated by MnCe@LR/AMs may hold potential clinical significance.

This study also found that MnCe@LR/AMs significantly regulated the polarization of intestinal macrophages, contributing to an improvement in the immune status of the organism (Figure 8). Previous studies have established *L. reuteri* as a key probiotic strain for intestinal inflammation management, demonstrating multifaceted mechanisms to coordinately regulate gut inflammation and microbiota homeostasis.[64] However, the distinct regulatory properties of MnCe@LR/AMs observed in this study differ from those of *L. reuteri* alone, indicating that their therapeutic mechanism extends beyond mere targeted delivery of *L. reuteri*. These findings suggest critical functional contributions from other components within the MnCe@LR/AMs system, which act synergistically to remodel the intestinal microenvironment for effective IBD intervention.

However, this study has several limitations: (a) The metabolic and immunomodulatory mechanisms of MnCe@LR/AMs require further systematic investigation and experimental validation; (b) A comparative analysis of hydrogel-based versus microsphere delivery systems is needed to evaluate their respective advantages in terms of stability and intestinal retention; (c) The generalizability of this probiotic delivery platform remains to be verified through extension to other therapeutic bacterial strains. In future studies, we will address these limitations to better elucidate the therapeutic mechanisms of MnCe@LR/AMs.

CONCLUSION

There is an urgent need for an IBD treatment that can effectively target inflammatory areas and restore intestinal homeostasis. To address this issue, we developed a hydrogel microsphere delivery system, MnCe@LR/AMs, with dual-targeting characteristics. This system combines the advantages of nanozymes and probiotics, not only effectively improving intestinal oxidative stress, but also significantly enhancing the colonization and survival rate of probiotics in the gut. Additionally, the dual-targeting system facilitates the precise targeting of the inflammatory area, greatly improving treatment efficiency. MnCe@LR/AMs effectively alleviated inflammation in IBD not only by reshaping the gut microbiota, but also by playing a significant role in regulating intestinal metabolism, gene expression, and immune responses. This study introduces a promising therapeutic strategy for the management of IBD, offering broad potential for application.

MATERIALS AND METHODS

Materials. Cerium(III) acetylacetonate hydrate and manganese(III) acetylacetonate hydrate were sourced from Sigma-Aldrich. H_2O_2 was procured from Sinopharm Chemical Reagent Co., Ltd. located in Shanghai, China. Sodium alginate was obtained from Sinopharm Chemical Reagent Co., Ltd. Dopamine was purchased from Shanghai Yuanye Bio-Technology Co., Ltd. SOD assay kits were acquired from Dojindo. FITC and Calcium chloride dihydrate were bought from Aladdin. All aqueous solutions employed in the experiments were prepared using deionized water from Millipore.

Characterization. XRD patterns were measured at a rate of 5° per minute using a diffractometer (Rigaku Ultima III from Japan and Bruker D8 advance from Germany) with Cu Kα radiation. The zeta potentials were measured on a Nano sizer ZS90 (Malvern). During zeta potential measurements, a vortex mixer was employed to ensure homogeneous dispersion of LR, MnCe@DSPE-PEG-NH_2, MnCe@LR, and MnCe@LR/AMs in deionized water, followed by immediate detection. The CAT-like activity of the nanozyme was measured by employing a dissolved oxygen meter (SevenExcellence Multiparameter, Mettler Toledo Co., Ltd.). The element content of Mn and Ce was measured by using a PerkinElmer Avio 500 ICP-AES).

Particle Size Distribution of MnCe@LR/AMs. First, the microsphere samples were imaged using an optical microscope (Olympus BX53, 100× objective), and three random fields of view (representing >100 microspheres in total) were captured. After excluding overlapping or irregular particles, the images were analyzed using ImageJ (v1.53a) to manually measure the diameters of all microspheres.

Bacterial Strains and Animals. The medical probiotic of *Limosilactobacillus reuteri* ATCC 23272 (*L. reuteri*, LR) was purchased from GemPharmaech (Nanjing, China) and cultured in MRS medium at 37 °C. Six-week-old male BALB/c mice were acquired from Nanjing Huimiaoxin Biotechnology Co., Ltd. (Nanjing, China). The mice were acclimated for 1 week in a temperature-and-humidity controlled environment, maintained on a strict 12 h light/12 h dark cycle with unrestricted access to sterile food and water prior to the experiments. Experiments involving mice and protocols were approved by the Ethics committee of Jingling Hospital (Ethics approval number: 2023JLHGZRDWLS−00078). All mice were housed in a specific-pathogen-free (SPF) facility.

Synthesis of CeO_2, Mn@CeO_2, MnCe@LR, MnCe@LR/AMs. 0.5 g of cerium(III) acetylacetonate hydrate was added to 15 mL of oleylamine. Subsequently, the mixture was heated from an initial temperature of 30 to 110 °C at 2 °C per minute. After reaching 110 °C, it was maintained at this temperature for 24 h. Obtained colloidal solution and cooled to room temperature. CeO_2 nanozymes were washed with acetone and then collected through centrifugation.

For the preparation of Mn@CeO_2 nanozymes, cerium(III) acetylacetonate hydrate and manganese(III) acetylacetonate hydrate (with a total mass of 0.5 g) were added to 15 mL of oleylamine. The mixture was heated from 30 to 110 °C at 2 °C per minute. Then, it was kept at 110 °C for 24 h. After obtaining a colloidal solution and cooled to room temperature, the Mn@CeO_2 nanozymes were washed with acetone and collected by centrifugation.

Next, 2 mL of CeO_2 and Mn@CeO_2 solutions in chloroform (10 mg/mL each) were mixed with 2 mL of DSPE-PEG-NH_2 solution in chloroform (20 mg/mL). Stir the mixture at room temperature until the chloroform has completely evaporated. The chloroform was removed under vacuum conditions. Subsequently, the PEG-modified CeO_2 and Mn@CeO_2 were dispersed in water. These PEG-modified CeO_2 and Mn@CeO_2

https://doi.org/10.1021/acsnano.5c08999
ACS Nano 2025, 19, 31619−31642

were utilized in all the experiments described in this paper. DSPE-PEG-NH_2 (MW 3400) was purchased from Ponsure Biological (Shanghai, China), purity 95%.

The LR was cultured in MRS medium at 37 °C. When the optical density at 600 nm (OD_{600}) reached 0.6, the LR culture medium was centrifuged and washed three times using PBS. The isolated LR was collected and stored in PBS (with a pH value of 7.4). At room temperature, Mn@CeO_2 was added to 1 mL of LR resuspended in PBS buffer, with the final concentration of the nanozyme being 20 μg/mL. The mixture was thoroughly mixed and then incubated at 4 °C for 1 h to obtain MnCe@LR. Subsequently, the mixture was added to the sodium alginate solution (10 mg/mL) and mixed thoroughly. Finally, the sodium alginate solution was loaded into a syringe connected to an electrostatic spraying system (T SLAMAN TCM6000) equipped with a LongerPump LSP01−3A microinjection pump. Electrospraying was conducted at room temperature using a 30G needle with a controlled flow rate of 500 μL/min and an applied voltage ranging from 9 to 15 kV. The alginate solution was electrosprayed into $CaCl_2$ solution (10% (w/v)), and thus MnCe@LR/AMs were prepared.

SOD- and Cat-Mimetic Catalytic Activity Assay. *Measurement of SOD-Like Activity.* The SOD-like activity of CeO_2 and Mn@CeO_2 nanozymes was evaluated by means of a SOD assay kit. Initially, 20 μL of the sample was mixed with 200 μL of 2-(4-iodophenyl)-3-(4-nitrophenyl)-5-(2,4-disulfophenyl)-2*H*-tetrazolium, monosodium salt. Subsequently, 20 μL of the enzyme working solution was added to the mixture, and they were cocultured at 37 °C for 20 min. Finally, used a microplate reader measured the absorbance at 450 nm.

Measurement of the Cat-Like Activity. The CAT-like activity of CeO_2 and Mn@CeO_2 nanozymes was measured by monitoring theamount of O_2 generated as well as the elimination of H_2O_2. First, the nanozyme sample was mixed with H_2O_2 (5 mM). Immediately after that, the amount of O_2 was recorded using a dissolved oxygen meter at intervals of 30 s.[65]

Alternatively, in a typical measurement procedure, the reaction system in a 96-well plate consisted of 5 μL, 90 μL of Tris buffer (with a concentration of 10 mM and a pH value of 8.5), 100 μL of dopamine (2 mg/mL), and 5 μL of hydrogen peroxide (with a concentration of 0.8 M). After added the solution into the plate, the plate was promptly transferred to an anaerobic device and incubated at 37 °C for 30 min. Finally, used a microplate reader measured the absorbance at 405 nm. To evaluate the CAT-like and SOD-like activities of MnCe@LR/AMs, the microspheres were incubated with SCF at ambient temperature for 4 h. Subsequently, the MnCe@LR/AMs were purified through three cycles of washing with deionized water, each involving centrifugation at 2000 × g for 10 min.

Measurement of the Intracellular CAT Activity and SOD Activity. RAW264.7 cells (1×10^5 cells per well) were seeded in a 6-well plate and incubated at 37 °C for 24 h. Subsequently, 20 μg/mL of CeO_2 and Mn@CeO_2 nanozymes were added to each well of the plate, followed by another 24 h of incubation. After that, the cells were washed three times with PBS (pH = 7.4). Then, 150 μM H_2O_2 was added to the each well and incubated for 30 min to stimulate them to generate intracellular ROS. After that, RAW264.7 cells were lysed in IP Lysis Buffer (Beyotime Biotechnology, China) at 1:100 dilution and phosphatase inhibitors (Beyotime Biotechnology, China) on ice for 30 min. Then centrifuged at 12000 rpm for 5 min to collect the supernatant. Measure the activities of SOD and CAT in the supernatant.

Measurement of Overall Antioxidant Activity. The overall antioxidant activity of the nanozyme was determined with respect to 2,2′-azinobis (3-ethyl benzothi-azoline-6-sulfonic acid) ammonium radical (ABTS+●). The experimental procedure was referred to a previous literature with certain modifications.

For the ABTS+● scavenging experiments, 10 mL of potassium persulfate ($K_2S_2O_8$) (2.45 mM) and 10 mL of ABTS (7 mM) aqueous solution were mixed, and the resulting solution was protected from light for 12 h to obtain an ABTS+● aqueous solution. Then, the nanozyme was added to the above ABTS+● aqueous solution (the concentration of which was diluted ten times), and the final concentration of the nanozyme was set at 0.1 mg/mL. At 37 °C, the mixture was incubated for a specific period of time (such as 0.5 or 1 h), and used a microplate reader measured the absorbance at 734 nm.[66]

Cytotoxicity Assay and ROS-Scavenging Effect of CeO_2. The intracellular ROS level was monitored by employing DCFH-DA as a fluorescent probe, with the aid of flow cytometry and laser scanning confocal microscopy. The DCFH-DA fluorescent probe has excitation and emission wavelengths of 488 and 525 nm, respectively.

Specifically, RAW264.7 cells (1×10^5 cells per well) were seeded in a 6-well plate and incubated at 37 °C for 24 h. Subsequently, 20 μg/mL of CeO_2 and Mn@CeO_2 nanozymes were added to each well of the plate, followed by another 24 h of incubation. After that, the cells were washed three times with PBS (pH = 7.4). Then, 150 μM H_2O_2 was added to the each well and incubated for 30 min to stimulate them to generate intracellular ROS. Subsequently, DCFH-DA (0.01 mM) dissolved in DMEM was added to each well for 30 min, and then the washing operation was repeated. Finally, the cells were photographed using a fluorescence microscope (Leica DMi8, Germany).

Measurement of Growth Curves of Coated Probiotics. To assess whether the nanocoating on the surface and alginate microsphere would affect the growth and proliferation of LR, the growth curves of native LR and MnCe@LR/AMs were measured. Briefly, the native LR and MnCe@LR/AMs were diluted in 3 mL of fresh MRS medium at a starting concentration of 1×10^8 CFU/mL and incubated at 37 °C with gentle shaking. Bacterial cultures were sampled at 0, 2, 4, 6, 8, 10, and 12 h, serially diluted, and spread on MRS agar plates. After 24 h aerobic incubation at 37 °C, colonies were counted.

Resistance Assay *In Vitro*. Equal amounts of native LR, MnCe@LR, and MnCe@LR/AMs were individually resuspended in simulated gastric fluid (SGF, pH = 1.3, purchased from Shanghai Yuanye Bio-Technology Co., Ltd.), simulated intestinal fluid (SIF, pH = 6.8, containing trypsin and phosphates, purchased from Shanghai Yuanye Bio-Technology Co., Ltd.), simulated colon fluid (SCF, pH = 7.4, purchased from Shanghai Yuanye Bio-Technology Co., Ltd.) and H_2O_2 (5 mM), and then incubated at 37 °C with gentle shaking. 100 μL of each sample was collected, washed with PBS, and plated on MRS agar with appropriate dilution at specified time points. Prior to plate counting or optical density measurement, MnCe@LR/AMs were pretreated with 100 mM sodium citrate buffer (MedChemExpress) for bacterial release.[67] Following 30 min incubation at room temperature, the samples were washed twice with PBS (pH 7.4) via centrifugation (3,000 × g, 5 min). Collected bacterial samples were resuspended at pre-dissociation concentrations, then subjected to plate count assays and optical density measurements. Colonies were counted after

https://doi.org/10.1021/acsnano.5c08999
ACS Nano 2025, 19, 31619−31642

incubation at 37 °C. The OD_{600} values were recorded at 0, 2, 4, 6, 8, and 10 h. After a 1 h incubation in SGF, 10 μL of each sample was taken, and morphological changes of encapsulated bacteria in response to environmental stress were observed using SEM.

Fluorescent Labeling of LR and Mn@CeO_2. *Preparation of FITC- Mn@CeO_2.* The DSPE-PEG-NH_2-modified Mn@CeO_2 was dispersed in water (1 mg/mL). Subsequently, FITC (1 mg/mL) was added to DSPE-PEG-NH_2-modified Mn@CeO_2 solution, and the mixture was stirred in the dark at room temperature for 2 h. Then, it was centrifuged at 10,000 rpm for 5 min, and the process was repeated until the supernatant was colorless. Obtained FITC-labeled Mn@CeO_2.

Preparation of DiR-LR. Add 10 μL DiR stock solution (1 mg/mL) to 1 mL of LR solution (1×10^9 CFU/mL), vortex and mix well, then incubate at 4 °C in the dark for 1 h. Then, it was centrifuged at 5000 rpm for 5 min, and the process was repeated until the supernatant was colorless. Obtained DiR-labeled LR. DiR was purchased from MedChemExpress (#HY-D1048), purity 99.89%. Then DiR-MnCe@LR/AMs was prepared according to the previous method.

Preparation of Cy5.5-Mn@CeO_2. 2 mL of the Mn@CeO_2 in chloroform (10 mg/mL) was mixed with 2 mL of DSPE-PEG-Cy5.5 in chloroform (20 mg/mL). Cy5.5-Mn@CeO_2 was obtained. The chloroform was removed by vacuum.

Preparation of FITC-LR. FITC was prepared as a 1 mM solution with anhydrous DMSO. The LR were grown in the MRS medium at 37 °C to OD_{600} = 0.6, then the prepared FITC solution was added to the LR culture medium diluted to OD_{600} = 0.3 and mixed (the final concentration of FITC was 100 μM), and then incubated at 37 °C for 0.5 h. The LR culture medium was centrifuged and washed three times with PBS. The isolated bacteria were collected and stored in PBS (pH 7.4). The FITC-LR were mixed with Cy5.5-Mn@CeO_2, incubated for 1 h, observed and photographed by laser confocal microscopy (Leica SP8 STED 3X, Germany).

Fluorescent Labeling of AM. Following the synthesis of MnCe@LR/AMs, the microspheres were washed three times with ultrapure water through centrifugation at 3000 rpm for 5 min each. The washed microspheres were then resuspended in ultrapure water and chemically activated by treatment with 10 mM EDC (1-ethyl-3-(3-(dimethylamino)propyl)carbodiimide) and 5 mM NHS (*N*-hydroxysuccinimide) under continuous stirring at room temperature for 1 h, followed by three additional washing cycles (3000 rpm, 5 min). For fluorescent labeling, the activated particles were incubated with 1 mg/mL NH_2−PEG-FITC and stirred protected from light at room temperature for 2−4 h. The resulting FITC-labeled MnCe@LR/AMs were collected by final centrifugation (3000 rpm, 5 min, three repeats) and stored at 4 °C protected from light to maintain fluorescence stability.

Quantitative Real-Time PCR Analysis. Fecal microbial DNA was isolated using a commercial stool DNA extraction kit (Tiangen Biotech, China). DNA concentrations were measured spectrophotometrically (NanoDrop, Agilent Technologies). Quantitative PCR was performed using SYBR Green chemistry (Thermo Fisher Scientific) on an ABI SteponePlus system, with LR abundance normalized to total bacterial 16S rRNA genes. Primer sets targeted: Universal bacteria: F-5′-ACTCCTACGGGAGGCAGCAGT-3′, *R*-5′-ATTACCGCGGCTGCTGG-3′; LR: F-5′-GCGTTGATGTTGTTGAAGGAATGAGCTTTG-3′, *R*-5′-CATCAGCAATGATTAAGAGAG CACGGCC-3′.[68] Gene expression was calculated using the comparative CT ($2^{-\Delta\Delta CT}$) method.

Cell Endocytosis. Raw264.7 cells were seeded in 24-well plates (5×10^3 cells per well) with round coverslips. FITC-AM labeled MnCe@LR/AMs were added to the cells, and the round coverslips were collected after 2 h. In the mannose competition assay, 20 mM mannose (Sigma-Aldrich, USA) was added to the medium and incubated for 24 h. After that, FITC-LR labeled MnCe@LR/AMs or FITC-Mn@CeO_2 labeled MnCe@LR/AMs were added to the cells. The round coverslips were collected after 24 h. Then washed the round coverslips three times with PBS (pH 7.4). DiD dye was added and incubated for 15 min, then washed the round coverslips three times with PBS (pH 7.4). Then the round coverslips were sealed with an antifluorescence quencher containing Hoechst. Fluorescence round coverslips were photographed using a laser confocal microscopy (Leica SP8 STED 3X, Germany).

Treatment of IBD mice.[69] DSS-induced UC model: Male BALB/c mice, aged 6 to 8 weeks, were randomly allocated into seven distinct groups: Health, DSS + PBS, DSS + LR, DSS + Mn@CeO_2, DSS + MnCe@LR, DSS + MnCe@LR/AMs, and DSS + 5-ASA. All groups, except the Health group, were first administered drinking water containing 2.5% DSS (w/v) for 7 days. Following this, they were orally gavaged with different materials for an additional 7 days. In the DSS + LR, DSS + MnCe@LR, and DSS + MnCe@LR/AMs groups, the LR concentration was 1×10^9 CFU/mL. Body weight, stool consistency, and fecal bleeding were assessed and recorded on a daily basis. The DAI was calculated as the sum of the stool consistency score (0−4), fecal bleeding score (0−4), and weight loss score (0−4). On day 15, the mice were euthanized, and major organs along with serum were collected. A one-centimeter segment of the distal colon was harvested for histological examination. Serum samples were obtained via retro-orbital sinus bleeding, and the concentrations of inflammatory cytokines were determined using ELISA kits sourced from Abcam.

TNBS-induced CD model: Male BALB/c mice (6−8 weeks old) were allowed to acclimate for 1 week. After hair removal on the back, TNBS was applied to induce sensitization. One week later, the mice were fasted for 12 h and anesthetized with isoflurane. On Day 7, 100 μL of TNBS (2.5 wt %, 50% ethanol) was administered rectally; control mice received 50% ethanol. After 24 h, mice were orally administered PBS, LR, Mn@CeO_2, MnCe@LR, or MnCe@LR/AMs (LR concentration 1×10^9 CFU/mL) for 5 days. Body weight, stool consistency, fecal blood, and DAI scores were recorded daily. On Day 13, the mice were euthanized, and major organs were collected.

Evaluation of the Targeted Adhesion to Inflamed Tissue Surfaces. To assess the inflammation-targeting ability of DiR-MnCe@LR/AMs, BALB/c mice were randomly allocated to four groups: Water + DiR-LR, DSS + DiR -LR, Water + DiR -MnCe@LR/AMs, and DSS + DiR -MnCe@LR/AMs. Mice were gavaged with equal doses of LR or LR encapsulated in microspheres (1×10^8 CFU). Mice were anesthetized with isoflurane at 0.5, 6, 12, 24, and 48 h postadministration, followed by *in vivo* fluorescence detection using the IVIS imaging system (PerkinElmer, Spectrum). At 48 h postadministration, the mice were euthanized, and their intestinal tracts were harvested for further imaging. For fluorescence intensity quantification, regions of interest (ROIs) were exclusively selected within colonic segments to ensure tissue-specific analysis.

https://doi.org/10.1021/acsnano.5c08999
ACS Nano 2025, 19, 31619−31642

Biosafety Evaluation. To investigate whether oral administration of MnCe@LR/AMs causes unwanted side effects, the mice were fed with MnCe@LR/AMs (LR concentration: 1×10^9 CFU/mL) once a day via oral gavage. After administrating for 7 days, the mice were executed under deep anesthesia. The heart, liver, spleen, lungs, and kidney samples were collected. The biosafety was confirmed by the histological study.

Western Blot Analysis. Proteins were isolated from frozen colon tissue using SDS-PAGE with 12% and 8% resolving gels. The separated proteins were subsequently electroblotted onto PVDF membranes for immunoblotting. Primary antibodies targeting ZO-1 (Abcam, UK), Occludin (Abcam, UK), and GAPDH (BOSTER, China) were applied according to the suppliers' protocols. Immunodetection was carried out using a Tanon EPS600 electrophoresis system, and protein bands were visualized with BioRad's Image Lab software (v4.0). Densitometric analysis was performed using ImageJ (version 1.53a) for semiquantitative evaluation.

Histopathology Studies. The tissue samples were immobilized in 4% paraformaldehyde, subsequently embedded in paraffin, and sectioned into 4-μm-thick slices for H&E staining and AB-PAS staining. The stained slides were then observed using a bright-field optical microscope. The colon's damage levels were evaluated according to the histopathology analysis with a scoring system.

Immunofluorescent Staining. Distal colon segments were fixed in 4% paraformaldehyde, then sectioned into serial slices. The slides were deparaffinized with xylene and rehydrated using an ascending ethanol series. Antigen retrieval was performed by incubating the sections in citrate buffer (0.01 M, pH 6.0, 0.05% Tween-20) in a steamer at 95 °C for 20 min. After three washes with TBS, the slides were permeabilized and blocked with 10% normal goat serum in 0.3% Triton X-100 PBST (PBS with 0.05% Tween-20) for 1 h at room temperature. For immunofluorescence staining, tissue sections were incubated with primary antibodies, followed by Alexa Fluor-conjugated secondary antibodies. Coverslips were mounted using an antifade reagent containing DAPI (Abcam, UK). The primary antibodies used were: anti-F4/80 (Servicebio, China), anti-CD86 (Abcam, UK), anti-CD206 (Abcam, UK), anti-Occludin (Proteintech, China), and anti-ZO-1 (Abcam, UK).

Gut Microbiota Profiling. Microbiome DNA isolation and 16S rDNA gene sequencing were conducted with the assistance of KAITAI-BIO Co., Ltd. Microbial DNA was extracted from mouse feces. The V3−V4 hypervariable region was amplified from the extracted DNA using specific primers fused with barcodes. HiFi sequences were filtered, clustered, and denoised using Qiime2 (Version 2023.2) to define operational taxonomic units (OTUs), followed by species annotation and abundance analysis using the SILVA138 database. Alpha diversity was evaluated using the Chao1 and Shannon indices, whereas beta diversity was examined through principal coordinate analysis (PCoA), employing the Bray−Curtis distance matrix as the basis for comparison. The Venn diagram for OTUs was generated using the R package VennDiagram. The evolutionary branching diagram was constructed using the LEfSe software. Microbiome functional prediction was performed using the Tax4Fun2 R package.

Transcriptome and Metabolome Analysis. *Transcriptome Sequencing Analysis.* RNA extraction and sequencing were performed with the assistance of KAITAI-BIO Co., Ltd. Extract RNA from the colonic tissues of mice in the DSS group and the MnCe@LR/AMs group. RNA sequencing was performed using an Illumina Novaseq 6000 (Illumina, USA). Differential expression analysis was performed using edgeR software, with p-values adjusted for multiple hypothesis testing, and statistical significance was determined at a threshold of $p < 0.05$. Pathway enrichment analysis of differentially expressed genes was performed utilizing the clusterProfiler software and the widely used GO and KEGG gene annotation databases.

Metabolome Sequencing and Data Analysis. Metabolite identification and analysis were conducted using LC-MS (liquid chromatography−mass spectrometry) with assistance from Company KAITAI-BIO Co., Ltd. LC analysis was conducted using a Vanquish UHPLC System (Thermo Fisher Scientific, USA). Metabolite detection was performed on an Orbitrap Exploris 120 (Thermo Fisher Scientific, USA) with an ESI ion source. PCA was employed to assess the clustering and dispersion of the samples. Metabolites with a p-value <0.05 from Student's t test and a VIP > 1.0 from OPLS-DA (first principal component) were considered significantly different metabolites (DMs). KEGG pathway enrichment analysis was conducted using a hypergeometric distribution-based method.

Verification of Hydrogel-Induced Macrophage Polarization. RAW264.7 cells were employed in a coculture experiment with MnCe@LR/AMs to assess their capacity to induce macrophage polarization. The proportions of M1 and M2 macrophages were determined using flow cytometry. RAW264.7 cells were seeded onto 6-well plates and treated with 100 ng/mL LPS to stimulate cell polarization. Following a 24 h incubation period, MnCe@LR/AMs was added to the plates. After 24 h, cells were harvested and analyzed by flow cytometry using a BD Canto II instrument. The collected cells were treated with FcR Blocking Reagent (BioLegend, USA) and incubated with F4/80-AF647 (BioLegend, USA), CD86-FITC (Thermo, USA), and CD206-PE (BioLegend, USA) antibodies. Subsequently, the cells were fixed using Fixation Buffer (BioLegend, USA) and permeabilized with Intracellular Staining Permeabilization Wash Buffer, also sourced from BioLegend (USA). Macrophages were initially selected based on F4/80 and CD86 expression (M1 marker), followed by the assessment of F4/80 and CD206 expression (M2 marker). Data were analyzed using Flowjo Analysis Software. Immunofluorescence staining was performed using primary antibodies for F4/80, CD86, and CD206. The stained cells were visualized and imaged using an inverted fluorescence microscope (Leica DMi8, Germany).

Isolation of Intestinal Laminapropria Cells. For the extraction of lamina propria cells from murine colonic tissue, initial dissection involved longitudinal opening of the colon segments, which were then extensively rinsed with chilled PBS to eliminate intestinal debris. The cleaned tissues were divided into 1 cm pieces and immersed in a washing medium composed of 10 mM HEPES, 1 mM DTT, and 30 mM EDTA. These fragments were shaken at 200 rpm at 37 °C through two consecutive 20 min cycles. Following this, the specimens were moved to specialized C-tubes containing enzymatic digestion medium and maintained at 37 °C with continuous shaking at 150 rpm for another 20 min. Mechanical dissociation was performed using a gentleMACS tissue dissociator (Miltenyi Biotec, 130−093−235) to generate a single-cell suspension. Finally, the isolated cells were combined with a Percoll-based separation medium and processed through buoyant density centrifugation for further purification.

Molecular Docking and MM/PBSA Calculations. The mannose receptor (PDB ID: 7JUB) was downloaded from the

https://doi.org/10.1021/acsnano.5c08999
ACS Nano 2025, 19, 31619−31642

Protein Data Bank (PDB), and molecular docking was conducted using the SMINA docking software. The PDB original ligand (methyl-mannoside), the MMGM alginate fragment, and the oligosaccharide monomer (mannopyranuronic acid), were docked to the receptor. Molecular dynamics simulations are performed with OpenMM, while ligand−receptor binding free energies are evaluated using the MM/PBSA method implemented in Amber's MMPBSA.py tool.

Statistical Analysis. The data are presented as means ± standard deviation (SD), and statistical differences between the two groups were assessed using an unpaired, two-tailed Student's *t* test. The statistical differences between the multiple groups were compared using the one-way ANOVA followed by Brown-Forsythe test. Grouped analysis was conducted using two-way ANOVA, followed by Tukey's multiple comparisons test for statistical comparisons. Regular analysis, Pearson correlation test and linear regression was analyzed with GraphPad Prism 10.3.0. Statistical significance was accepted at a P-value threshold of 0.05 in all cases. Significance levels were indicated as follows: * for $p < 0.05$, ** for $p < 0.01$, *** for $p < 0.001$, and **** for $p < 0.0001$.

ASSOCIATED CONTENT

Supporting Information

The Supporting Information is available free of charge at https://pubs.acs.org/doi/10.1021/acsnano.5c08999.

Potential mechanism of *L. reuteri* ameliorating IBD; Schematic diagram of the nanozyme structures; HRTEM images and XPS of CeO_2 and Mn@CeO_2; cytotoxicity of CeO_2 and Mn@CeO_2; evaluation of the biocompatibility; zeta potentials; particle size distribution of MnCe@LR/AMs; loading efficiency of Mn and Ce elements; ROS scavenging capacity of Mn@CeO_2 and CeO_2; antioxidant activities *in vitro*; fluorescence images of AM and LR following 1 h incubation in SGF; Growth curves in MRS medium; IVIS images of mice following DiR administration. AB-PAS staining images. Relative abundance of selected genus; relative abundance of selected species; Linear discriminant analysis; principal component analysis; two-way orthogonal PLS analysis; linear regression plots and Pearson correlation analysis; immune infiltration analysis; bright-field microscopy images during incubation in DMEM medium; Internalization of LR and Mn@CeO_2 by macrophages; flow cytometry analysis of macrophage polarization; binding poses of MMA receptors with mannopyranuronic acid; therapeutic Efficacy in CD; biosafety; MM/PBSA calculations of the binding capacities (PDF)

AUTHOR INFORMATION

Corresponding Authors

Xinying Wang − *Clinical Nutrition Service Center, Department of General Surgery, Jinling Hospital, Affiliated Hospital of Medical School, Nanjing University, Nanjing 210002, China;* orcid.org/0000-0002-6611-9210; Email: wangxinying@nju.edu.cn

Hui Wei − *College of Engineering and Applied Sciences, Nanjing National Laboratory of Microstructures, Jiangsu Key Laboratory of Artificial Functional Materials, Nanjing University, Nanjing 210023, China;* orcid.org/0000-0003-0870-7142; Email: weihui@nju.edu.cn

Authors

Pinwen Zhou − *Clinical Nutrition Service Center, Department of General Surgery, Jinling Hospital, Affiliated Hospital of Medical School, Nanjing University, Nanjing 210002, China;* orcid.org/0000-0003-1268-2806

Qi Sun − *College of Engineering and Applied Sciences, Nanjing National Laboratory of Microstructures, Jiangsu Key Laboratory of Artificial Functional Materials, Nanjing University, Nanjing 210023, China*

Longchang Huang − *Clinical Nutrition Service Center, Department of General Surgery, Jinling Hospital, Affiliated Hospital of Medical School, Nanjing University, Nanjing 210002, China*

Yufei Xia − *Medical School of Southeast University, Nanjing 210009, China*

Jiaqi Wang − *Clinical Nutrition Service Center, Department of General Surgery, Jinling Hospital, Affiliated Hospital of Medical School, Nanjing University, Nanjing 210002, China*

Dongze Mo − *College of Engineering and Applied Sciences, Nanjing National Laboratory of Microstructures, Jiangsu Key Laboratory of Artificial Functional Materials, Nanjing University, Nanjing 210023, China*

Christopher J. Butch − *Department of Biomedical Engineering, College of Engineering and Applied Sciences, Nanjing University, Nanjing 210023, China;* orcid.org/0000-0003-3112-0470

Chenmei Li − *Department of Biomedical Engineering, College of Engineering and Applied Sciences, Nanjing University, Nanjing 210023, China*

Li Zhang − *Clinical Nutrition Service Center, Department of General Surgery, Jinling Hospital, Affiliated Hospital of Medical School, Nanjing University, Nanjing 210002, China*

Xuejin Gao − *Clinical Nutrition Service Center, Department of General Surgery, Jinling Hospital, Affiliated Hospital of Medical School, Nanjing University, Nanjing 210002, China*

Complete contact information is available at: https://pubs.acs.org/10.1021/acsnano.5c08999

Author Contributions

#P.Z., Q.S., and L.H. contributed equally to this work. The manuscript was written through contributions of all authors. All authors have given approval to the final version of the manuscript.

Funding

This study was funded by the Jiangsu Province Key Research and Development Project (grant no. BE2022822) and the National Natural Science Foundation of China (grant no. 82370900, grant no. 82170575 and grant no. 81770531).

Notes

The authors declare no competing financial interest.

ACKNOWLEDGMENTS

We acknowledge BioRender (BioRender.com) for providing the platform to create scientific illustrations used in this study.

REFERENCES

(1) Danne, C.; Skerniskyte, J.; Marteyn, B.; Sokol, H. Neutrophils: from IBD to the gut microbiota. *Nat. Rev. Gastroenterol. Hepatol.* **2024**, *21* (3), 184−197.

(2) Lavelle, A.; Sokol, H. Gut microbiota-derived metabolites as key actors in inflammatory bowel disease. *Nat. Rev. Gastroenterol. Hepatol.* **2020**, *17* (4), 223−237.

(3) (a) Iatsenko, I.; Boquete, J. P.; Lemaitre, B. Microbiota-Derived Lactate Activates Production of Reactive Oxygen Species by the Intestinal NADPH Oxidase Nox and Shortens Drosophila Lifespan. *Immunity* **2018**, *49* (5), 929−942. (b) Sun, Y.; Wang, X.; Li, L.; Zhong, C.; Zhang, Y.; Yang, X.; Li, M.; Yang, C. The role of gut microbiota in intestinal disease: from an oxidative stress perspective. *Front. Microbiol.* **2024**, *15* (15), 1328324. Neish, A. S. Redox signaling mediated by the gut microbiota. *Free Radic. Res.* **2013**, *47* (11), 950−957.

(4) Tian, T.; Wang, Z.; Zhang, J.; Egea, J. Pathomechanisms of oxidative stress in inflammatory bowel disease and potential antioxidant therapies. *Oxid. Med. Cell. Longevity* **2017**, *2017* (1), 4535194.

(5) Windsor, J. W.; Kaplan, G. G. Evolving Epidemiology of IBD. *Curr. Gastroenterol.* **2019**, *21*, 1−9.

(6) (a) Bernstein, C. N.; Fried, M.; Krabshuis, J. H.; Cohen, H.; Eliakim, R.; Fedail, S.; Gearry, R.; Goh, K. L.; Hamid, S.; Khan, A. G.; et al. World Gastroenterology Organization Practice Guidelines for the Diagnosis and Management of IBD in 2010. *Inflamm. Bowel Dis.* **2010**, *16* (1), 112−124. (b) Lautenschläger, C.; Schmidt, C.; Fischer, D.; Stallmach, A. Drug delivery strategies in the therapy of inflammatory bowel disease. *Adv. Drug Delivery Rev.* **2014**, *71*, 58−76. (c) Cader, M. Z.; Kaser, A. Finding the right target for drug-resistant inflammatory bowel disease. *Nat. Med.* **2021**, *27* (11), 1870−1871.

(7) (a) Plichta, R.; Graham, D.; Subramanian, S.; Xavier, R. J. Therapeutic Opportunities in Inflammatory Bowel Disease: Mechanistic Dissection of Host-Microbiome Relationships - ScienceDirect. *Cell* **2019**, *178* (5), 1041−1056. (b) Suez, J.; Zmora, N.; Segal, E.; Elinav, E. The pros, cons, and many unknowns of probiotics. *Nat. Med.* **2019**, *25* (5), 716−729. (c) Gou, H. Z.; Zhang, Y. L.; Ren, L.; Li, Z. J.; Zhang, L. How do intestinal probiotics restore the intestinal barrier? *Front. Microbiol.* **2022**, *13* (13), 929346.

(8) Han, S.; Lu, Y.; Xie, J.; Fei, Y.; Zheng, G.; Wang, Z.; Liu, J.; Lv, L.; Ling, Z.; Berglund, B.; Yao, M. Probiotic Gastrointestinal Transit and Colonization After Oral Administration: A Long Journey. *Front. Cell. Infect. Microbiol.* **2021**, *11* (1), 609722.

(9) (a) Wei, H.; Wang, E. Nanomaterials with enzyme-like characteristics (nanozymes): next-generation artificial enzymes. *Chem. Soc. Rev.* **2013**, *42* (14), 6060−6093. (b) Huang, Y.; Ren, J.; Qu, X. Nanozymes: Classification, Catalytic Mechanisms, Activity Regulation, and Applications. *Chem. Rev.* **2019**, *119* (6), 4357−4412. (c) Wei, H; Wang, E. Nanomaterials with enzyme-like characteristics (nanozymes): next-generation artificial enzymes. *Chem. Soc. Rev.* **2013**, *42* (14), 6060−6093.

(10) (a) Yang, M.; Liu, J.; Liu, C.; Zhang, H.; Li, S.; Zhang, T.; Yu, Z.; Chi, X.; Zhang, Z.; Du, Z. Programmable Food-Derived Peptide Coassembly Strategies for Boosting Targeted Colitis Therapy by Enhancing Oral Bioavailability and Restoring Gut Microenvironment Homeostasis. *ACS Nano* **2025**, *19* (1), 600−620. (b) Li, A. N.; Li, S.; Zhang, Y. J.; Xu, X. R.; Chen, Y. M.; Li, H. B. Resources and Biological Activities of Natural Polyphenols. *Nutrients* **2014**, *6* (12), 6020−6047.

(11) Ma, Y.; Zhao, J.; Deng, Z.; Gao, B.; Xu, C.; Yan, X.; Yang, M.; Zhang, Y.; Xu, Q.; Zhang, M.; Xu, C. Macrophage-biomimetic liposomes delivery of carbon dots nanozymes ameliorate ulcerative colitis by modulating inflammation pathways and remodeling the redox microenvironment. *Chem. Eng. J.* **2023**, *477*, 146796.

(12) Zhou, S.; Cai, H.; He, X.; Tang, Z.; Lu, S. Enzyme-mimetic antioxidant nanomaterials for ROS scavenging: design, classification, and biological applications. *Coord. Chem. Rev.* **2024**, *500*, 215536.

(13) Zhao, S.; Li, Y.; Liu, Q.; Li, S.; Cheng, Y.; Cheng, C.; Sun, Z.; Du, Y.; Butch, C. J.; Wei, H. An orally administered CeO2@ montmorillonite nanozyme targets inflammation for inflammatory bowel disease therapy. *Adv. Funct. Mater.* **2020**, *30* (45), 2004692.

(14) Han, S. I.; Lee, S.-W.; Cho, M. G.; Yoo, J. M.; Oh, M. H.; Jeong, B.; Kim, D.; Park, O. K.; Kim, J.; Namkoong, E.; Jo, J.; et al. Epitaxially Strained CeO2/Mn3 O4 Nanocrystals as an Enhanced Antioxidant for Radioprotection. *Adv. Mater.* **2020**, *32* (31), No. e2001566.

(15) Zhang, Y.; Yang, F.; Gao, R.; Dai, W.-L. Manganese-doped CeO2 nanocubes as highly efficient catalysts for styrene epoxidation with TBHP. *Appl. Surf. Sci.* **2019**, *471*, 767−775.

(16) Pernomian, L.; Duarte-Silva, M.; de Barros Cardoso, C. R. The Aryl Hydrocarbon Receptor (AHR) as a Potential Target for the Control of Intestinal Inflammation: Insights from an Immune and Bacteria Sensor Receptor. *Clin. Rev. Allergy Immunol.* **2020**, *59* (3), 382−390.

(17) Dong, F.; Hao, L.; Wang, L.; Huang, Y. Clickable nanozyme enhances precise colonization of probiotics for ameliorating inflammatory bowel disease. *J. Controlled Release* **2024**, *373*, 749−765.

(18) Cao, F.; Jin, L.; Gao, Y.; Ding, Y.; Wen, H.; Qian, Z.; Zhang, C.; Hong, L.; Yang, H.; Zhang, J.; Tong, Z. Artificial-enzymes-armed Bifidobacterium longum probiotics for alleviating intestinal inflammation and microbiota dysbiosis. *Nat. Nanotechnol.* **2023**, *18* (6), 617−627.

(19) Karim, A.; Rehman, A.; Feng, J.; Noreen, A.; Assadpour, E.; Kharazmi, M. S.; Lianfu, Z.; Jafari, S. M. Alginate-based nanocarriers for the delivery and controlled-release of bioactive compounds. *Adv. Colloid Interface Sci.* **2022**, *307*, 102744.

(20) Huang, C.; Xie, T.; Liu, Y.; Yan, S.; OuYang, F.; Zhang, H.; Lei, L.; He, D.; Wei, H.; Yu, C.-Y. A Sodium Alginate-Based Multifunctional Nanoplatform for Synergistic Chemo-Immunotherapy of Hepatocellular Carcinoma. *Adv. Mater.* **2023**, *35* (33), No. e2301352.

(21) (a) Chang, D.; Lei, J.; Cui, H.; Lu, N.; Sun, Y.; Zhang, X.; Gao, C.; Zheng, H.; Yin, Y. Disulfide cross-linked nanospheres from sodium alginate derivative for inflammatory bowel disease: Preparation, characterization, and in vitro drug release behavior. *Carbohydr. Polym.* **2012**, *88* (2), 663−669. (b) Lima, D. S.; Tenório-Neto, E. T.; Lima-Tenório, M. K.; Guilherme, M. R.; Scariot, D. B.; Nakamura, C. V.; Muniz, E. C.; Rubira, A. pH-responsive alginate-based hydrogels for protein delivery. *J. Mol. Liq.* **2018**, *262*, 29−36.

(22) Yu, Z.; Chen, J.; Liu, Y.; Meng, Q.; Liu, H.; Yao, Q.; Song, W.; Ren, X.; Chen, X. The role of potential probiotic strains Lactobacillus reuteri in various intestinal diseases: New roles for an old player. *Front. Microbiol.* **2023**, *14*, 1095555.

(23) (a) Li, M.; Ding, Y.; Wei, J.; Dong, Y.; Wang, J.; Dai, X.; Yan, J.; Chu, F.; Zhang, K.; Meng, F.; et al. Gut microbiota metabolite indole-3-acetic acid maintains intestinal epithelial homeostasis through mucin sulfation. *Gut Microbes.* **2024**, *16* (1), 2377576. (b) Wang, G.; Huang, S.; Cai, S.; Yu, H.; Wang, Y.; Zeng, X.; Qiao, S. Lactobacillus reuteri Ameliorates Intestinal Inflammation and Modulates Gut Microbiota and Metabolic Disorders in Dextran Sulfate Sodium-Induced Colitis in Mice. *Nutrients* **2020**, *12* (8), 2298. (c) Dias, A. M. M.; Douhard, R.; Hermetet, F.; Regimbeau, M.; Lopez, T. E.; Gonzalez, D.; Masson, S.; Marcion, G.; Chaumonnot, K.; Uyanik, B.; et al. Lactobacillus stress protein GroEL prevents colonic inflammation. *J. Gastroenterol.* **2021**, *56* (5), 442−455.

(24) Ma, Y.; Gao, W.; Zhang, Z.; Zhang, S.; Tian, Z.; Liu, Y.; Ho, J. C.; Qu, Y. Regulating the surface of nanoceria and its applications in heterogeneous catalysis. *Surf. Sci. Rep.* **2018**, *73* (1), 1−36.

(25) Oe, T.; Dechojarassri, D.; Kakinoki, S.; Kawasaki, H.; Furuike, T.; Tamura, H. Microwave-Assisted Incorporation of AgNP into Chitosan-Alginate Hydrogels for Antimicrobial Applications. *J. Funct. Biomater.* **2023**, *14* (4), 199.

(26) Mittal, M.; Siddiqui, M. R.; Tran, K.; Reddy, S. P.; Malik, A. B. Reactive oxygen species in inflammation and tissue injury. *Antioxid. Redox Signal.* **2014**, *20* (7), 1126−1167.

(27) Lv, W.; Jiang, G.; Lin, X.; Qian, M.; Huang, R.; Li, Z.; Liu, H.; Lin, D.; Wang, Y. An Unusual Application of Multifunctional Nanozyme Derived from COF: Augmenting Chemoimmunotherapy while Attenuating Cardiotoxicity. *Adv. Funct. Mater.* **2024**, *35*, 2412862.

(28) Begley, M.; Gahan, C. G. M.; Hill, C. The interaction between bacteria and bile. *FEMS Microbiol. Rev.* **2005**, *29* (4), 625−651.

(29) Perše, M.; Cerar, A. Dextran sodium sulphate colitis mouse model: traps and tricks. *J. Biomed Biotechnol.* **2012**, *2012*, 718617.

(30) Xu, J.; Chu, T.; Yu, T.; Li, N.; Wang, C.; Li, C.; Zhang, Y.; Meng, H.; Nie, G. Design of Diselenide-Bridged Hyaluronic Acid Nanoantioxidant for Efficient ROS Scavenging to Relieve Colitis. *ACS Nano* **2022**, *16* (8), 13037−13048.

(31) Shan, Y.; Lee, M.; Chang, E. B. The Gut Microbiome and Inflammatory Bowel Diseases. *Annu. Rev. Med.* **2022**, *73*, 455−468.

https://doi.org/10.1021/acsnano.5c08999
ACS Nano 2025, 19, 31619−31642

(32) de la cuesta-Zuluaga, J.; Kelley, S. T.; Chen, Y.; Escobar, J. S.; Mueller, N. T.; Ley, R. E.; McDonald, D.; Huang, S.; Swafford, A. D.; Knight, R.; Thackray, V. G.; et al. Age- and Sex-Dependent Patterns of Gut Microbial Diversity in Human Adults. *mSystems* **2019**, *4* (4), No. e00261.
(33) Xu, H.-M.; Huang, H.-L.; Liu, Y.-D.; Zhu, J.-Q.; Zhou, Y.-L.; Chen, H.-T.; Xu, J.; Zhao, H.-L.; Guo, X.; Shi, W.; Nie, Y.-Q.; et al. Selection strategy of dextran sulfate sodium-induced acute or chronic colitis mouse models based on gut microbial profile. *BMC Microbiol.* **2021**, *21* (1), 279.
(34) Zhou, Y.; Zhi, F. Lower Level of Bacteroides in the Gut Microbiota Is Associated with Inflammatory Bowel Disease: A Meta-Analysis. *BioMed. Res. Int.* **2016**, *2016*, 5828959.
(35) Singh, V.; Lee, G.; Son, H.; Koh, H.; Kim, E. S.; Unno, T.; Shin, J.-H. Butyrate producers, "The Sentinel of Gut": Their intestinal significance with and beyond butyrate, and prospective use as microbial therapeutics. *Front. Microbiol.* **2022**, *13*, 1103836.
(36) Zheng, Y.; Zhang, Z.; Tang, P.; Wu, Y.; Zhang, A.; Li, D.; Wang, C.-Z.; Wan, J.-Y.; Yao, H.; Yuan, C.-S. Probiotics fortify intestinal barrier function: a systematic review and meta-analysis of randomized trials. *Front. Immunol.* **2023**, *14*, 1143548.
(37) Liu, J.; Zong, C.; Yu, X.; Ding, Y.; Chang, B.; Wang, R.; Sang, L. Alanyl-Glutamine (Ala-Gln) Ameliorates Dextran Sulfate Sodium (DSS)-Induced Acute Colitis by Regulating the Gut Microbiota, PI3K-Akt/NF-κB/STAT3 Signaling, and Associated Pulmonary Injury. *ACS Infect. Dis.* **2023**, *9* (4), 979−992.
(38) Zhao, J.; Wang, D.; Li, X.; Yang, Q.; Chen, H.; Zhong, Y.; Zeng, G. Free nitrous acid serving as a pretreatment method for alkaline fermentation to enhance short-chain fatty acid production from waste activated sludge. *Water Res.* **2015**, *78*, 111−120.
(39) Lupp, C.; Robertson, M. L.; Wickham, M. E.; Sekirov, I.; Champion, O. L.; Gaynor, E. C.; Finlay, B. B. Host-mediated inflammation disrupts the intestinal microbiota and promotes the overgrowth of Enterobacteriaceae. *Cell Host. Microbe.* **2007**, *2* (2), 119−129.
(40) (a) Li, Y.; Liu, N.; Ge, Y.; Yang, Y.; Ren, F.; Wu, Z. Tryptophan and the innate intestinal immunity: crosstalk between metabolites, host innate immune cells, and microbiota. *Eur. J. Immunol.* **2022**, *52* (6), 856−868. (b) Ma, N.; Ma, X. Dietary amino acids and the gut-microbiome-immune axis: physiological metabolism and therapeutic prospects. *Compr. Rev. Food Sci. Food Saf.* **2019**, *18* (1), 221−242.
(41) (a) Waclawiková, B.; Bullock, A.; Schwalbe, M.; Aranzamendi, C.; Nelemans, S. A.; van Dijk, G.; El Aidy, S. Gut bacteria-derived 5-hydroxyindole is a potent stimulant of intestinal motility via its action on L-type calcium channels. *PLoS Biol.* **2021**, *19* (1), No. e3001070. (b) Li, F.; Jiang, L.; Pan, S.; Jiang, S.; Fan, Y.; Jiang, C.; Gao, C.; Leng, Y.; David, L. A. Multi-omic Profiling Reveals that Intra-abdominal-Hypertension-Induced Intestinal Damage Can Be Prevented by Microbiome and Metabolic Modulations with 5-Hydroxyindoleacetic Acid as a Diagnostic Marker. *MSystems* **2022**, *7* (3), No. e0120421.
(42) Lee, R.; Britz-McKibbin, P. Differential rates of glutathione oxidation for assessment of cellular redox status and antioxidant capacity by capillary electrophoresis-mass spectrometry: an elusive biomarker of oxidative stress. *Anal. Chem.* **2009**, *81* (16), 7047−7056.
(43) el bouhaddani, S.; Houwing-Duistermaat, J.; Salo, P.; Perola, M.; Jongbloed, G.; Uh, H.-W. Evaluation of O2PLS in Omics data integration. *BMC Bioinf.* **2016**, *17* (Suppl 2), S11.
(44) Ruth, M. R.; Field, C. J. The immune modifying effects of amino acids on gut-associated lymphoid tissue. *J. Anim Sci. Biotechnol.* **2013**, *4* (1), 27.
(45) Albaugh, V. L.; Mukherjee, K.; Barbul, A. Proline Precursors and Collagen Synthesis: Biochemical Challenges of Nutrient Supplementation and Wound Healing. *J. Nutr.* **2017**, *147* (11), 2011−2017.
(46) Han, X.; Ding, S.; Jiang, H.; Liu, G. Roles of Macrophages in the Development and Treatment of Gut Inflammation. *Front. Cell Dev. Biol.* **2021**, *9*, 625423.
(47) van der Zande, H. J. P.; Nitsche, D.; Schlautmann, L.; Guigas, B.; Burgdorf, S. The Mannose Receptor: From Endocytic Receptor and Biomarker to Regulator of (Meta)Inflammation. *Front. Immunol.* **2021**, *12*, 765034.
(48) Li, D.-F.; Yang, M.-F.; Xu, H.-M.; Zhu, M.-Z.; Zhang, Y.; Tian, C.-M.; Nie, Y.-Q.; Wang, J.-Y.; Liang, Y.-J.; Yao, J.; et al. Nanoparticles for oral delivery: targeted therapy for inflammatory bowel disease. *J. Mater. Chem. B* **2022**, *10* (31), 5853−5872.
(49) Scheiffele, F.; Fuss, I. J. Induction of TNBS colitis in mice. *Curr. Protoc. Immunol.* **2002**, *49* (1), 19.
(50) (a) Allegretti, J. R.; Khanna, S.; Mullish, B. H.; Feuerstadt, P. The Progression of Microbiome Therapeutics for the Management of Gastrointestinal Diseases and Beyond. *Gastroenterology* **2024**, *167* (5), 885−902. (b) Huang, L.; Wang, P.; Liu, S.; Deng, G.; Qi, X.; Sun, G.; Gao, X.; Zhang, L.; Zhang, Y.; Xiao, Y. Gut microbiota-derived tryptophan metabolites improve total parenteral nutrition-associated infections by regulating Group 3 innate lymphoid cells. *iMeta* **2025**, *2* (4), No. e70007.
(51) Wang, M.; Yang, J.; Li, M.; Wang, Y.; Wu, H.; Xiong, L.; Sun, Q. Enhanced viability of layer-by-layer encapsulated Lactobacillus pentosus using chitosan and sodium phytate. *Food Chem.* **2019**, *285*, 260−265.
(52) Yang, J.; Xiao, S.; Deng, J.; Li, Y.; Hu, H.; Wang, J.; Lu, C.; Li, G.; Zheng, L.; Wei, Q.; Zhong, J. Oxygen vacancy-engineered cerium oxide mediated by copper-platinum exhibit enhanced SOD/CAT-mimicking activities to regulate the microenvironment for osteoarthritis therapy. *J. Nanobiotechnol.* **2024**, *22* (1), 491.
(53) Pirmohamed, T.; Dowding, J. M.; Singh, S.; Wasserman, B.; Heckert, E.; Karakoti, A. S.; King, J. E.; Seal, S.; Self, W. T. Nanoceria exhibit redox state-dependent catalase mimetic activity. *Chem. Commun.* **2010**, *46* (16), 2736−2738.
(54) Wang, G.; Zhang, J.; He, X.; Zhang, Z.; Zhao, Y. Ceria nanoparticles as enzyme mimetics. *Chin. J. Chem.* **2017**, *35* (6), 791−800.
(55) Campbell, C. T.; Peden, C. H. Oxygen vacancies and catalysis on ceria surfaces. *Science* **2005**, *309* (5735), 713−714.
(56) Cummings, R. D. The mannose receptor ligands and the macrophage glycome. *Curr. Opin. Struct. Biol.* **2022**, *75*, 102394.
(57) Gan, J.; Dou, Y.; Li, Y.; Wang, Z.; Wang, L.; Liu, S.; Li, Q.; Yu, H.; Liu, C.; Han, C.; Huang, Z. Producing anti-inflammatory macrophages by nanoparticle-triggered clustering of mannose receptors. *Biomaterials* **2018**, *178*, 95−108.
(58) (a) Wu, J.; Xia, C.; Liu, C.; Zhang, Q.; Xia, C. The role of gut microbiota and drug interactions in the development of colorectal cancer. *Front. Pharmacol.* **2023**, *14*, 1265136. (b) Tourret, J.; Willing, B. P.; Dion, S.; MacPherson, J.; Denamur, E.; Finlay, B. B. Immunosuppressive Treatment Alters Secretion of Ileal Antimicrobial Peptides and Gut Microbiota, and Favors Subsequent Colonization by Uropathogenic Escherichia coli. *Transplantation* **2017**, *101* (1), 74−82.
(59) Fu, X.; Liu, Z.; Zhu, C.; Mou, H.; Kong, Q. Nondigestible carbohydrates, butyrate, and butyrate-producing bacteria. *Crit. Rev. Food Sci. Nutr.* **2019**, *59* (sup1), S130−S152.
(60) He, J.; Zhang, P.; Shen, L.; Niu, L.; Tan, Y.; Chen, L.; Zhao, Y.; Bai, L.; Hao, X.; Li, X.; et al. Short-Chain Fatty Acids and Their Association with Signalling Pathways in Inflammation, Glucose and Lipid Metabolism. *Int. J. Mol. Sci.* **2020**, *21* (17), 6356.
(61) Sartor, R. B. Therapeutic manipulation of the enteric microflora in inflammatory bowel diseases: antibiotics, probiotics, and prebiotics. *Gastroenterology* **2004**, *126* (6), 1620−1633.
(62) (a) Recharla, N.; Geesala, R.; Shi, X.-Z. Gut Microbial Metabolite Butyrate and Its Therapeutic Role in Inflammatory Bowel Disease: A Literature Review. *Nutrients* **2023**, *15* (10), 2275. (b) Louis, P.; Flint, H. J. Formation of propionate and butyrate by the human colonic microbiota. *Environ. Microbiol.* **2017**, *19* (1), 29−41.
(63) Qazi, A.; Sharma, A.; Amin, F.; Khin, E.; Calzadilla, N.; Golovchenko, N.; Edelblum, K.; Comiskey, S.; Saksena, S.; Alrefai, W.; Gill, R. Altered fecal and serum aromatic amino acids and transporters in small intestinal inflammation. *Physiology* **2023**, *38* (S1), 5734810.
(64) (a) Wang, G.; Huang, S.; Cai, S.; Yu, H.; Wang, Y.; Zeng, X.; Qiao, S. Lactobacillus reuteri ameliorates intestinal inflammation and modulates gut microbiota and metabolic disorders in dextran sulfate

https://doi.org/10.1021/acsnano.5c08999
ACS Nano 2025, 19, 31619−31642

sodium-induced colitis in mice. *Nutrients* **2020**, *12* (8), 2298. (b) Hu, R.; Lin, H.; Wang, M.; Zhao, Y.; Liu, H.; Min, Y.; Yang, X.; Gao, Y.; Yang, M. Lactobacillus reuteri-derived extracellular vesicles maintain intestinal immune homeostasis against lipopolysaccharide-induced inflammatory responses in broilers. *J. Animal Sci. Biotechnol.* **2021**, *12* (1), 25. (c) Wu, H.; Xie, S.; Miao, J.; Li, Y.; Wang, Z.; Wang, M.; Yu, Q. Lactobacillus reuteri maintains intestinal epithelial regeneration and repairs damaged intestinal mucosa. *Gut Microbes.* **2020**, *11* (14), 997–1014.

(65) Lin, A.; Liu, Q.; Zhang, Y.; Wang, Q.; Li, S.; Zhu, B.; Miao, L.; Du, Y.; Zhao, S.; Wei, H. A Dopamine-Enabled Universal Assay for Catalase and Catalase-Like Nanozymes. *Anal. Chem.* **2022**, *94* (30), 10636–10642.

(66) Wang, Q.; Cheng, C.; Zhao, S.; Liu, Q.; Zhang, Y.; Liu, W.; Zhao, X.; Zhang, H.; Pu, J.; Zhang, S.; Zhang, H.; et al. A Valence-Engineered Self-Cascading Antioxidant Nanozyme for the Therapy of Inflammatory Bowel Disease. *Angew. Chem., Int. Ed.* **2022**, *61* (27), No. e202201101.

(67) Atia, A.; Gomaa, A.; Fernandez, B.; Subirade, M.; Fliss, I. Study and Understanding Behavior of Alginate-Inulin Synbiotics Beads for Protection and Delivery of Antimicrobial-Producing Probiotics in Colonic Simulated Conditions. *Probiotics Antimicrob. Proteins* **2018**, *10* (2), 157–167.

(68) Mu, Q.; Swartwout, B. K.; Edwards, M.; Zhu, J.; Lee, G.; Eden, K.; Cabana-Puig, X.; McDaniel, D. K.; Mao, J.; Abdelhamid, L.; Brock, R. M.; et al. Regulation of neonatal IgA production by the maternal microbiota. *Proc. Natl. Acad. Sci. U. S. A.* **2021**, *118* (9), No. e2015691118.

(69) Wirtz, S.; Popp, V.; Kindermann, M.; Gerlach, K.; Weigmann, B.; Fichtner-Feigl, S.; Neurath, M. F. Chemically induced mouse models of acute and chronic intestinal inflammation. *Nat. Protoc.* **2017**, *12* (7), 1295–1309.

https://doi.org/10.1021/acsnano.5c08999
ACS Nano 2025, 19, 31619–31642